Chemical Geology 708 (2026) 123328

Contents lists available at ScienceDirect

Chemical Geology

journal homepage: www.elsevier.com/locate/chemgeo

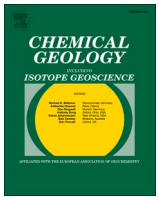

Experimental and thermodynamic constraints on the magmatic variables governing pre-eruptive conditions at Hunga volcano: Development of a new equilibrium orthopyroxene-clinopyroxene thermometer

Enrico Califano [a,b,*], Silvio Mollo [b,c], Marco Brenna [a], Alessio Pontesilli [c], Jie Wu [d], Patricia Marks [e], Dennis Eul [e], Marcus Nowak [e], Shane J. Cronin [d], Fabrizio Di Fiore [c], Alessandro Vona [f], Sumith Abeykoon [g], Danilo Di Genova [h], Claudia Romano [f], Piergiorgio Scarlato [c]

[a] Department of Geology, University of Otago; Dunedin, 9054, New Zealand
[b] Department of Earth Sciences, Sapienza – University of Rome; Rome 00185, Italy
[c] Section of Roma 1, National Institute of Geophysics and Volcanology; Rome 00143, Italy
[d] School of Environment, University of Auckland, Auckland 1010, New Zealand
[e] Department of Geosciences, Eberhard Karls University Tübingen; Tübingen 72074, Germany
[f] Department of Science, University of Roma Tre, Roma 00146, Italy
[g] School of Science and Technology, Geology Division, University of Camerino, Camerino 62032, Italy
[h] Institute of Science, Technology and Sustainability for Ceramics (ISSMC), National Research Council of Italy (CNR), Faenza 48018, Italy

ARTICLE INFO

Editor: Marco Fiorentini

Keywords:
Hunga volcano
Isobaric-isothermal crystallization experiments
Thermodynamic modeling
Plagioclase-based hygrometry
Orthopyroxene-clinopyroxene thermometry

ABSTRACT

The cataclysmic eruption of Hunga volcano (Tonga-Kermadec arc system) on 15 January 2022, the most powerful explosive volcanic event of the 21st century, underscores the critical need to constrain the pre-eruptive magmatic conditions governing arc volcanoes with shallow marine calderas. In this study, we present results from isobaric-isothermal crystallization experiments conducted on a basaltic andesite representative of primitive magmas at Hunga volcano. Experimental runs were performed at pressures of 200 and 300 MPa, over a temperature range of 1000–1130 °C, melt water contents of 0.6–6.4 wt%, and oxygen fugacities between +0.7 and + 3.4 log units relative to the nickel-nickel oxide buffer. Temperature and melt-water content are the primary controls on modal phase assemblages and compositional trends in the experimental charges, exerting a dominant influence on the cotectic crystallization of clinopyroxene and plagioclase, as well as on the stability of orthopyroxene and abundance of magnetite. By integrating experimental data with thermodynamic modeling, orthopyroxene-clinopyroxene thermometry, and plagioclase-based hygrometry, we document that both pre-2022 and 2022 eruptive products at Hunga volcano reflect the differentiation of basaltic andesitic to andesitic magmas at pre-eruptive temperatures of ~1050–1130 °C and melt-water contents up to ~3 wt%. Under the investigated experimental conditions, however, extensive crystallization of plagioclase and magnetite at ~1000 °C drives the host basaltic andesitic melt toward more evolved dacitic compositions. Dacites have not been reported at Hunga volcano, but they occur in low-temperature, magnetite-bearing phenocryst assemblages on other Tongan islands, particularly in the northern part of the arc. Collectively, our experimental-thermodynamic approach provides compelling evidence for polythermal and polybaric plumbing systems at intra-oceanic arc volcanoes, highlighting the pivotal role of phase stability and mineral chemistry in controlling the differentiation pathways of magmas and the transition from tholeiitic to calc-alkaline affinity.

1. Introduction

Hunga volcano is situated in the southwestern Pacific, within the intra-oceanic Tonga-Kermadec island arc (Fig. 1a), which formed by the westward subduction of the Pacific oceanic lithosphere beneath the Australian Plate (Schellart et al., 2006). The volcanic arc extends for

* Corresponding author at: Department of Geology, University of Otago, Dunedin, 9054, New Zealand.
E-mail address: enrico.califano@uniroma1.it (E. Califano).

https://doi.org/10.1016/j.chemgeo.2026.123328
Received 1 September 2025; Received in revised form 20 February 2026; Accepted 23 February 2026
Available online 26 February 2026

more than 3000 km in a north-northeast direction from New Zealand and is underlain by oceanic crust ~20-km-thick (Contreras-Reyes et al., 2011; Crawford et al., 2003). Magmatism is dominated by tholeiites and basaltic andesites, with less abundant andesites, dacites and rhyolites, and sporadic occurrences of boninites (e.g., Ewart et al., 1973, 1998).

Hunga Tonga and Hunga Ha'apai are two small, uninhabited islands, each ~2 km in length and rising up to 114 m above sea level (Fig. 1b). They represent the emergent summit of the largely submarine Hunga volcano and are situated along the rim of a submerged caldera (Fig. 1b), representing remnants of a volcanic cone destroyed during at least two caldera-forming eruptions preceding the 2022 explosive event (Cronin et al., 2017). The volcanic products consist predominantly of basaltic andesitic to andesitic lava flows and pyroclastic deposits, intruded by dykes (Bryan et al., 1972; Brenna et al., 2022). Historical volcanic activity has been characterized by shallow, magma-water interaction typical of Surtseyan-style eruptions, occurring around the caldera rim. Small-scale subaerial and submarine eruptions have been recorded in 1912, 1937, 1988, and more recently in 2009 and 2014–2015 (Bryan et al., 1972; Gatliff et al., 1991; Cronin et al., 2017).

On 15 January 2022, Hunga volcano produced the most powerful explosive eruption of the 21st century to date (Fig. 1c), with a volcanic explosivity index (VEI) of 6 and an eruption plume that exceeded 58 km in height, reaching into the mesosphere (Proud et al., 2022; Vergoz et al., 2022). The cataclysmic eruption generated acoustic waves that circled the globe multiple times (Wright et al., 2022), triggered significant ionospheric perturbations (Astafyeva et al., 2022), and caused a global fast-traveling tsunami (Kubota et al., 2022). Satellite gravity data (Le Mevèl et al., 2023) and volatile contents in melt inclusions (Wu et al., 2025) comparatively suggest that a shallow magma reservoir located between 2 and 6 km depth was tapped by the eruption. As a result, the central 4 km-wide-portion of the volcano collapsed inward, forming an ~1000-m-deep caldera, consistent with the evacuation of more than 6.8 km^3 of magma (Wu et al., 2025 and references therein).

This extraordinary eruptive event revealed the potential of small, shallow submarine calderas to trigger globally significant hazards. Understanding the magmatic processes that control the transition from storage to eruption in such settings remains a fundamental goal in petrology and volcanology. The magmatic variables governing the evolution of submarine to subaerial arc volcanoes that produce large-scale explosions have yet to be fully constrained, primarily due to the scarcity of experimental data linking pre-eruptive storage conditions to eruptive behavior. Consequently, the respective roles of pressure (P), temperature (T), oxygen fugacity (fO_2), and melt-water content (H_2O^{melt}) in driving phase stability, melt differentiation, and redox evolution of intra-oceanic arc magmas need to be investigated and clarified. Determining these parameters is crucial not only to reconstruct

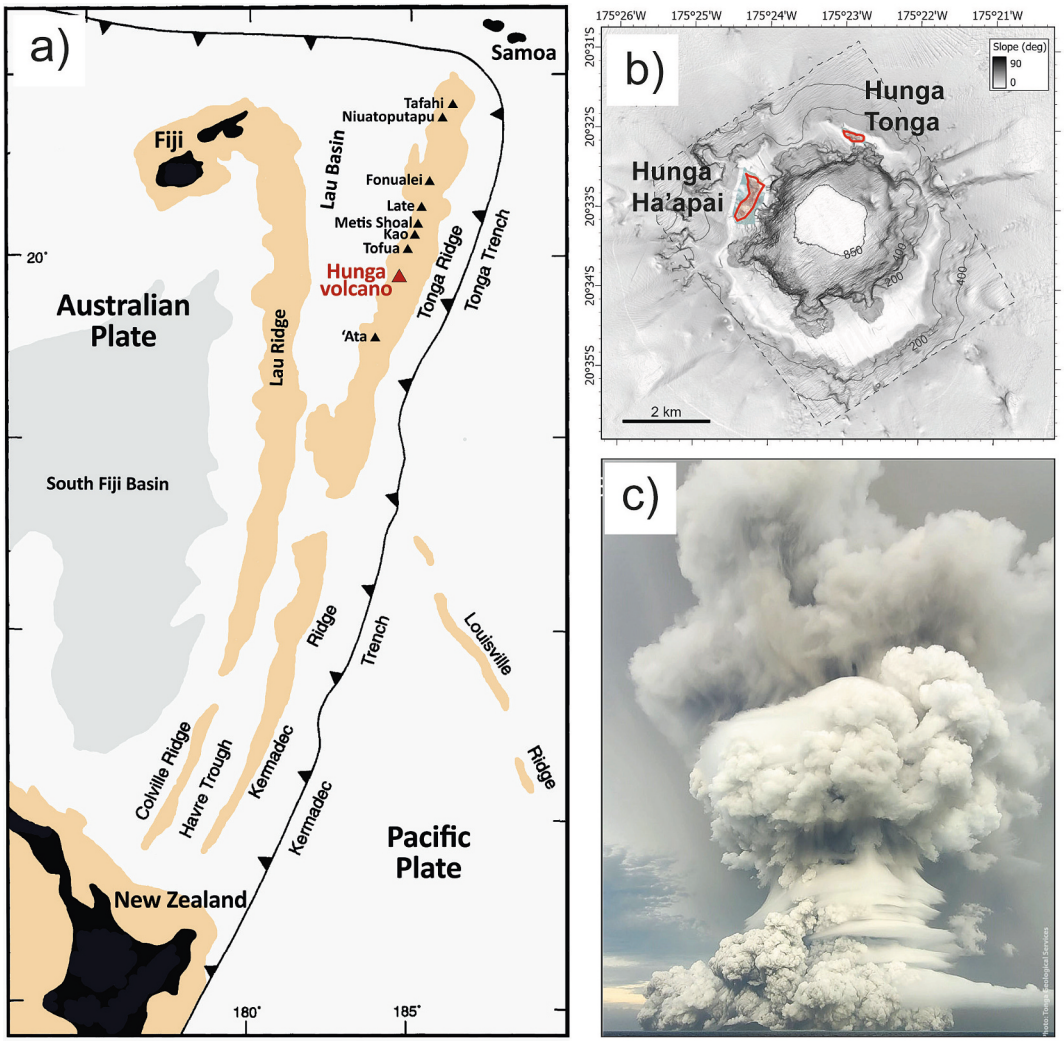

Fig. 1. Location of Hunga volcano within the intra-oceanic Tonga-Kermadec island arc and its tectonic setting (a). 2022 bathymetric map and volcanic edifice morphology showing the two emergent islands of Hunga Tonga and Hunga Ha'apai, situated along the rim of a submerged caldera (b). Eruptive column generated by the cataclysmic 2022 eruption (c).

the pre-eruptive history of Hunga volcano but also to improve predictive models for other arc systems where magma dynamics across the plumbing system may influence eruption style and magnitude.

In this study, we address these gaps through a comprehensive suite of isobaric-isothermal crystallization experiments performed on a basaltic andesite representative of primitive Hunga magmas. By systematically varying P, T, fO_2, and H_2O^{melt}, we isolate and identify the key physico-chemical parameters that control mineral phase relations and melt differentiation paths. Integrating these experimental results with thermodynamic modeling, orthopyroxene-clinopyroxene thermometry, and plagioclase-based hygrometry, we quantify the pre-eruptive conditions that prevailed in the pre-2022 and 2022 magmas at Hunga volcano. Our findings provide new constraints on how subvolcanic plumbing systems beneath intra-oceanic arcs operate, elucidating the processes that modulate magma evolution as a function of the type and abundance of crystallizing mineral phases.

2. Methods

2.1. Experiments

The first set of experiments (Table 1) was conducted using a non-end-loaded piston cylinder (PC) apparatus (QUICKpress model, Depths of the Earth Co.), installed at the HP-HT Laboratory of Experimental Volcanology and Geophysics of the Istituto Nazionale di Geofisica e Vulcanologia (Italy). The PC is equipped with a 25 mm assembly specifically designed for low-pressure, high-temperature experiments (Masotta et al., 2012), consisting of a 10.8 mm outer diameter graphite furnace, a 16 mm outer diameter borosilicate glass insulator, and a NaCl cell. The assembly was cold pressurized to a nominal pressure 10% higher than that desired for the experiment. After heating, pressure was gradually decreased to the final value of 300 MPa, with an uncertainty of ±25 MPa. A factory-calibrated S-type (Pt10%Rh-Pt) thermocouple (error ± 3 °C) was used to monitor the temperature. The experiments were first heated 50 °C above the target temperature (Table 1) at a constant rate of 80 °C min^{-1}. Following a dwell time of 1 h, the temperature was lowered to the target value using the same rate. After 24 h, a rapid quench of ~100 °C s^{-1} was imposed by switching off the current. This experimental strategy was designed following the work of Mollo et al. (2013a), who investigated both equilibrium crystallization and mineral growth kinetics in a basaltic magma. In that study, equilibrium cation partitioning between minerals and melts was assessed by comparing two heating protocols in a 1-atm furnace under controlled redox conditions: 1) direct heating of the experimental capsule from room temperature to the target temperatures of 1000 and 1100 °C and 2) cooling from a *superliquidus* temperature of 1250 °C down to the same target temperatures. Both approaches produced identical phase proportions and compositions for clinopyroxene, plagioclase, and titanomagnetite, confirming equilibrium conditions. In the present study, the

Table 1
Summary of experimental conditions, phase assemblages, and modal proportions. Additional details are provided in Supplementary Material 1.

Run#	P (MPa)	$T_{initial}$ (°C)	$t_{initial}$ (h)	T_{dwell} (°C)	t_{dwell} (h)	logfO_2	H_2O^{melt} (wt %)	Mt (vol %)	Cpx (vol %)	Pl (vol %)	Opx (vol %)	Gl (vol %)
Piston cylinder experiments												
PC-300-1130-2.8	300	1180	1	1130	24	−7.3	2.8	1	4	–	–	95
PC-300-1100-4.2	300	1150	1	1100	24	−7.4	4.2	1	3	–	–	95
PC-300-1100-3.5	300	1150	1	1100	24	−7.6	3.5	2	4	–	–	94
PC-300-1075-4.9	300	1125	1	1075	24	−7.6	4.9	1	5	–	–	94
PC-300-1075-3.7	300	1125	1	1075	24	−7.9	3.7	2	7	5	–	86
PC-300-1075-1.9	300	1125	1	1075	24	−8.1	1.9	2	13	11	–	74
PC-300-1075-0.6	300	1125	1	1075	24	−8.3	0.6	2	16	13	–	69
PC-300-1050-5.5	300	1100	1	1050	24	−7.8	5.5	2	6	0	–	92
PC-300-1050-4.1	300	1100	1	1050	24	−8.2	4.1	2	8	5	3	83
PC-300-1050-3.4	300	1100	1	1050	24	−8.2	3.4	3	10	8	4	75
PC-300-1050-1.1	300	1100	1	1050	24	−8.6	1.1	3	16	13	5	63
PC-300-1025-4.1	300	1075	1	1025	24	−8.4	4.1	3	11	9	3	74
PC-300-1000-6.4	300	1050	1	1000	24	−8.4	6.4	5	5	6	–	84
PC-300-1000-5.7	300	1050	1	1000	24	−8.6	5.7	5	7	9	2	77
PC-300-1000-5.3	300	1050	1	1000	24	−8.6	5.3	5	10	13	2	70
PC-300-1000-3.8	300	1050	1	1000	24	−8.8	3.8	6	14	21	5	54
Internally heated pressure vessel experiments												
IHPV-200-1100-1.0	200	1150	1	1100	24	−7.0	1.0	1	4	1	–	94
IHPV-200-1075-4.1	200	1125	1	1075	24	−5.8	4.1	1	5	–	–	94
IHPV-200-1075-3.1	200	1125	1	1075	24	−5.9	3.1	1	7	3	–	89
IHPV-200-1075-1.7	200	1125	1	1075	24	−6.6	1.7	2	9	7	–	82
IHPV-200-1050-5.6	200	1100	1	1050	24	−6.5	5.6	2	5	–	–	93
IHPV-200-1050-2.5	200	1100	1	1050	24	−7.6	2.5	3	9	7	1	80
IHPV-200-1050-1.7	200	1100	1	1050	24	−7.7	1.7	3	12	10	2	73
IHPV-200-1000-5.3	200	1050	1	1000	24	−6.6	5.3	5	8	10	2	75
IHPV-200-1000-4.6	200	1050	1	1000	24	−6.8	4.6	5	10	12	3	70
IHPV-200-1000-4.3	200	1050	1	1000	24	−6.9	4.3	5	11	14	4	66
IHPV-200-1000-4.0	200	1050	1	1000	24	−6.9	4.0	6	12	18	4	60
IHPV-200-1000-3.5	200	1050	1	1000	24	−7.0	3.5	6	13	19	5	57

preheating step 50 °C above the target temperature was introduced to promote crystal growth, as supported by numerous literature studies (e.g., Fabbrizio et al., 2021). The imposed heating and cooling rate of 80 °C min^{-1} was sufficiently rapid to suppress disequilibrium crystallization during temperature changes between the initial and final stages of the experiment (Mollo et al., 2013b; Mollo and Hammer, 2017). The experiments were performed using $Au_{80}Pd_{20}$ capsules (8 mm length, 2.7 mm inner diameter) loaded with the starting material. Variable amounts of deionized water were also added using a micro-syringe. A basaltic andesite representative of primitive whole rock compositions at Hunga volcano was selected as starting material, double melted at 1600 °C for 1 h in a 1-atm furnace under the oxygen fugacity of air, and then finely ground into a glassy powder (Supplementary Material 1). Ten electron microprobe analyses of this glass yielded an average composition (in wt %) of SiO_2 = 55.33 (±0.10), TiO_2 = 0.45 (±0.03), Al_2O_3 = 16.71 (±0.08), FeO = 9.04 (±0.07), MnO = 0.13 (±0.02), MgO = 5.16 (±0.06), CaO = 11.20 (±0.09), Na_2O = 1.61 (±0.07), K_2O = 0.29 (±0.04), and P_2O_5 = 0.08 (±0.02). Within the analytical uncertainty of the electron microprobe measurements, the starting glass composition is virtually identical to the whole rock composition of the natural sample (Supplementary Material 1). Because the redox condition imposed at 1 atm was higher than those effectively attained in the high-pressure experimental charges (see below), the kinetics of the iron oxidation reaction in silicate melts must be evaluated. Raman spectroscopy and X-ray absorption near edge structure (XANES) experiments at the iron K-edge by Magnien et al. (2008) suggest that little time is required for the $Fe^{3+}/\Sigma Fe$ ratio to reach 99% equilibrium at T = 1000–1300 °C for anhydrous alkali-bearing melts (i.e., 20 to 150 s for sample thicknesses of ~190–240 μm). Iron redox diffusivity is ~0.5 log units faster than that measured for Ca in anhydrous jadeitic and albitic melts (Magnien et al., 2008). In comparison, diffusion experiments by Mungall et al. (1999) indicate that the addition of ~3.7 wt% H_2O to haplogranitic melts significantly increases the diffusivity of Ca by ~1.7 log units. Based on these data from high-viscosity silicic systems, iron redox equilibrium was likely achieved in our low-viscosity, basaltic andesitic melt within ~3.5 h, even in charges with minimum water content. Within this short timeframe, growth rate models for magnetite (Pontesilli et al., 2019), clinopyroxene (Moschini et al., 2021), and plagioclase (Moschini et al., 2023) indicate that crystals would remain small, with sizes restricted to 4, 15, and 20 μm, respectively. Oxygen fugacity was not independently buffered but was instead controlled indirectly by the intrinsic hydrogen fugacity of the experimental apparatus. The hydrogen fugacity was controlled by permeation of hydrogen through the capsule walls between the fluid phase in the PC ($fH_2^{apparatus}$) and hydrogen in the inner capsule in either an excess fluid phase ($fH_2^{capsule}$) or in the melt ($aH_2^{capsule}$). Using Mössbauer spectroscopy, Masotta et al. (2012) determined that the intrinsic oxygen fugacity of the piston cylinder is two log units above the nickel-nickel oxide buffer ($fO_2^{apparatus}$ = NNO+2). Assuming that the PC was water-saturated under these oxidizing conditions (Iacovino et al., 2013; Marxer et al., 2022), the value of $fH_2^{apparatus}$ can be quantified through the dissociation reaction of water. The equilibrium constant (K_w) for the reaction $[H_2 + 1/2O_2] \leftrightarrow [H_2O]$ is given by the expression: $K_w = fH_2O^{apparatus} / \left[fH_2^{apparatus} \left(fO_2^{apparatus}\right)^{1/2}\right]$. Among the numerous formalisms and equations available in the literature for the thermodynamic properties of water, we followed the methodology of Iacovino et al. (2013), where K_w is derived from Robie et al. (1978) at the appropriate pressure and temperature, while $fH_2O^{apparatus}$ is obtained by the Redlich-Kwong equation of Holloway (1977), later refined by Flowers (1979). As reported in King et al. (2000), the value of $fH_2O^{capsule}$ can be determined with the same equilibrium reaction, provided that $fH_2^{capsule} = fH_2^{apparatus}$ due to the rapid diffusion of hydrogen, and knowing the activity of water in the inner capsule ($aH_2O^{capsule}$). The condition $fO_2^{capsule} = fO_2^{apparatus}$ = NNO+2 is attained only when the experimental charges reach water-saturation ($aH_2O^{capsule}$ = 1). In water-undersaturated charges ($aH_2O^{capsule} < 1$), the value of $fO_2^{capsule}$ decreases relative to $fO_2^{apparatus}$, following the relationship (e.g., King et al., 2000; Marxer et al., 2022): $\log fO_2^{capsule} = \log fO_2^{apparatus} + 2\log\left(aH_2O^{capsule}\right)$, where the second term is inherently negative for $aH_2O^{capsule} < 1$. As detailed later, the water content of residual glasses from this study was measured by Raman spectrometry. The water activity was then calculated using the thermodynamic model of Burnham (1979), according to the procedure outlined by Holloway and Blank (1994) (Supplementary Material 1). The oxygen fugacity determined across the experimental charges spans from −8.8 to −7.3 log units (Table 1). Propagation of electron microprobe analytical uncertainties into the melt compositional parameters of the Burnham (1979) model indicates that the calculated oxygen fugacities are accurate to within ±0.3 log units. For $\Delta NNO = \log fO_2^{capsule} - \log fO_2^{NNO}$, where $\log fO_2^{NNO}$ represents the oxygen fugacity at the NNO buffer calculated by the equation of Huebner and Sato (1970) for the experimental *P-T* conditions, the redox state of the experimental charges ranges between ΔNNO+0.7 and ΔNNO+1.7 (Supplementary Material 1). Results from these calculations compare well with those of Cooper et al. (2022), who reported oxygen fugacities varying from ΔNNO to ΔNNO+2.6 for magmas erupted from seven volcanoes along the volcanic front of the Tonga arc, based on the vanadium partitioning between olivine and melt. The experimental oxygen fugacities were also validated by evaluating Fe solubility in the $Au_{80}Pd_{20}$ alloy with the solution model of Barr and Grove (2010) (Supplementary Material 1). The difference between the two methods is relatively small, varying from 0.1 to 0.3 log units, for FeO concentrations in the capsule walls measured by electron microprobe between ~0.1 to ~0.8 wt%. Mass balance calculations indicate that the loss of iron from the melt into the $Au_{80}Pd_{20}$ capsule remains low, not exceeding 9%, due to the predominantly oxidizing conditions of the experimental charges.

The second set of experiments (Table 1) was conducted using an internally heated pressure vessel (IHPV) installed at the Department of Geosciences, University of Tübingen (Germany). The IHPV operates with argon as pressure medium and is equipped with a rapid quench setup. Crystallization experiments were performed at 200 MPa using $Au_{80}Pd_{20}$ capsules (12 mm length, 2.7 mm inner diameter) loaded with the powdered primitive basaltic andesite, with varying amounts of deionized water added. Two control thermocouples (S-type, Pt10%Rh-Pt) recorded a thermal gradient of less than 10 °C along the capsule. The experimental samples were first heated 50 °C above the target temperature at a constant rate of 25 °C min^{-1}. Following a dwell time of 1 h, the temperature was lowered to the target value (Table 1) using a rate of 2 °C min^{-1} and then maintained for 24 h. The experiments were quenched at ~97 °C s^{-1} by switching off the furnace (Marks and Nowak, 2025). According to Berndt et al. (2002), the intrinsic redox state imposed by the IHPV to the water-saturated charges is governed by the MnO-Mn_3O_4 buffering reaction, corresponding to ~NNO+4 under the experimental *P-T* conditions. For water-undersaturated charges from this study, the redox state was determined following the same methodology described above. Results from calculations indicate that the overall oxygen fugacity calculated for the experimental charges varies from −5.8 to −7.7 (Table 1). Compared to the NNO buffer equation of Huebner and Sato (1970), the redox state of the experimental charges ranges between ΔNNO+1.2 and ΔNNO+3.4 (Supplementary Material 1). The discrepancy with calculations based on the iron solution model of Barr and Grove (2010) remains minimal (Supplementary Material 1), varying from 0.1 to 0.2 log units, for FeO concentrations in the capsule walls between ~0.1 to ~0.7 wt%. The iron loss from the melt into the $Au_{80}Pd_{20}$ capsule does not exceed 8%. Convergence of redox estimates for both PC and HIPV experiments, obtained using two independently calibrated thermodynamic models, indicates that melt components (including H_2O) reached equilibrium within the capsule over the

duration of the experiments.

Our calculation indicates that the complementary design of both PC and IHPV systems enabled exploration of a broader range of redox states within the experimental capsules. For convenience and consistency across experimental charges, the labels of PC and IHPV experiments follow the format *PC-300-XXXX-Y.Y* and *IHPV-200-XXXX-Y.Y*, respectively, where *XXXX* represents the experimental temperature and *Y.Y* denotes the melt-water content (Table 1).

2.2. Analyses

Photomicrographs of experimental products were collected in backscattered electron (BSE) mode using field emission gun-scanning electron microscope FE-SEM JEOL JSM-6500F, equipped with an energy-dispersive spectrometer (EDS) detector and installed at the HP-HT Laboratory of Experimental Volcanology and Geophysics of the Istituto Nazionale di Geofisica e Vulcanologia (Italy). Multiple photomicrographs were randomly collected across the entire width and length of the experimental product, covering a representative area ranging from 50% to 70% of the total sample surface, depending on the degree of crystallization under the experimental conditions investigated. The acquired BSE photomicrographs were processed to determine the mineral and glass volume proportions (Table 1) using NIH ImageJ software and reduced to binary images (i.e., black and white color) by grey level thresholding (i.e., image segmentation). The uncertainty associated with the segmentation process was evaluated by adding/subtracting pixel layers around each crystal in the binary image (cf. Pontesilli et al., 2019).

Major and minor oxide concentrations of crystals and glasses were obtained on polished and carbon-coated epoxy disks at the School of Environment, University of Auckland (New Zealand), using a JEOL-8530F field emission gun electron probe micro-analyzer (FEG-EPMA) equipped with five wavelength dispersive spectrometers. All these analyses can be found in the Supplementary Material 1. An accelerating potential of 15 kV was employed for all the analyses. The beam current was tuned at 8 nA for Si, Na, and K, and 20 nA for all other elements. The spot size ranged from 1 to 15 μm for plagioclase, while a 1 μm spot size was used for clinopyroxene, orthopyroxene, and titanomagnetite. Glasses were analyzed using a defocused beam of 15 μm. Counting times were 20 s on-peak and 10 s for background, except for Na and K (10 s peak per 5 s background) that were analyzed first to minimize alkali migration. Matrix correction was undertaken using a ZAF (Z: atomic number; A: absorption; F: fluorescence) procedure. Calibration standards were: VG-A99 (Si-TAP), rutile (Ti-LIF), anorthite (Al-TAP), fayalite (Fe-LIF), spessartine (Mn-LIF), Springwater olivine (Mg-TAP), wollastonite (Ca-PET), jadeite (Na-TAP), orthoclase OR-1 (K-PET), and orthophosphate $HoPO_4$ (P-PET) for glass; jadeite (Si-TAP, Na-LIF), rutile (Ti-PET), anorthite (Al-TAP), fayalite (Fe-LIF), spessartine (Mn-LIF), Springwater olivine (Mg-TAP), wollastonite (Ca-PET), and jadeite (Na-TAP) for clinopyroxene and orthopyroxene; orthoclase OR-1 (Si-TAP, K-PET), rutile (Ti-LIF), anorthite (Al-TAP, Ca-PET), fayalite (Fe-LIF), spessartine (Mn-LIF), Springwater olivine (Mg-TAP), and albite (Na-TAP) for plagioclase; rutile (Ti-LIF), kyanite (Al-TAP), magnetite (Fe-LIF), spessartine (Mn-LIF), and magnesiochromite (Mg-LIF, Cr-LIF) for titanomagnetite. Secondary standards used for routine quality control were: Smithsonian glasses VG-2, VG-A99, and VG-568 for glass and plagioclase; MAC olivine and augite for clinopyroxene and orthopyroxene; Smithsonian ilmenite and magnetite for oxides. Accuracy and precision from secondary standards were typically better than 1–3% for oxides with abundance >1 wt%. For oxides with abundance <1 wt%, accuracy was typically better than 1–6%. Analytical precision determined using the FEG-EPMA outputted uncertainty based on counting statistics for each analysis was better than 1% and 6% for oxides with abundances >10 wt% and < 10 wt%, respectively. For mapping, an accelerating voltage of 15 kV and a current of 20 nA were used, with 2 μm per pixel resolution and 150 ms acquisition time per pixel, measuring up to 5 elements per analysis (Supplementary Material 1).

Raman spectra were acquired at EVPLab of Roma Tre University (Italy) using a Jobin Yvon LABRAM HR800 Horiba micro-Raman spectrometer, equipped with an attenuated doubled Nd3:YAG laser (532 nm wavelength) and calibrated using a silicon standard. The operating conditions were 600 grooves per mm grating density, confocal hole opening 300 μm, and slit aperture 200 μm, exposure time of 60 s (3 times). The laser power at source was 60 mW (0.15 mW on the sample surface). A nominal spatial resolution of ~5 μm^2 was obtained with the 100× objective. For each sample, 3 spectra were acquired to assess data reproducibility. The backscattered Raman radiation was collected over ranges of 100–1500 cm^{-1} and 2700–4000 cm^{-1}, corresponding to low-wavenumber (*LW*) silicate and high-wavenumber (*HW*) water regions, respectively (Supplementary Material 1). The Matlab© code developed by Di Genova et al. (2017) was employed to perform Long correction (Long, 1977), background subtraction, and *HW/LW* parameterization (i.e., Raman band area ratio). The calibration fit [$(HW/LW)_{Raman}$ against $H_2O_{Standard}$, error ± 0.25 wt% H_2O] of Moschini et al. (2023) was used for the quantification of melt-water content (Table 1). The amount of dissolved water was also calculated by the difference method of Devine et al. (1995) as: $H_2O_{EMPA} = 100 - \Sigma_{EMPA}$, where Σ_{EMPA} is the sum of anhydrous oxide components measured in the glass with microprobe. For dissolved water contents up to ~7.5 wt%, recent studies indicate that H_2O_{EMPA} is overestimated by only ~10% compared to more precise H_2O_{Raman} (Bonechi et al., 2021; Moschini et al., 2023). According to these studies, the difference between H_2O_{EMPA} and H_2O_{Raman} ranges from 0.3 to 0.6 wt% for melt-water contents varying from 0.6 to 6.4 wt% in our experimental products (Supplementary Material 1).

To verify the spatial distribution of water in silicate glasses within the $Au_{80}Pd_{20}$ capsules, a further set of Raman spectroscopy measurements was carried out at the Gateway Laboratory of Amorphous and Structured Solids and Melts (GLASS) of CNR–ISSMC in Rome. Single Raman spectra and 2D maps were acquired using a confocal Raman microscope (WITec - Alpha300R) equipped with a 457 nm blue solid-state laser. The Raman spectrometer was calibrated using a silicon standard and operated with 600 grooves per mm grating density and a Blaze wavelength (BLZ) of 500 nm for both single spectra and the 2D maps (Supplementary Material 1). To assess potential spatial water gradients within the silicate glass, multiple single Raman spectra were randomly collected along both the vertical and horizontal directions of the $Au_{80}Pd_{20}$ capsules. A 50× objective was used to collect both the silicate and water scattering regions from 0 to 4000 cm^{-1}. Each spectrum was acquired with an integration time of 10 s and five accumulations, using a laser power of 8 mW on the sample surface. 2D Raman maps were obtained from a selected 100 × 50 μm region primarily composed of silicate glass with a few embedded crystals (Supplementary Material 1). A spatial resolution of ~1.5 μm^2 was achieved, and both optical images and spatial Raman data were collected using 50× objective. To compensate for surface topography effects on the 2D Raman maps, a three-point calibration was applied within the region of interest. Raman spectra were recorded across the silicate and water regions with an integration time of 4 s per spectrum. After data acquisition, cosmic ray removal and background subtraction were performed. The spatial distribution of water in the 2D Raman map was determined based on the peak width of the water band from ~3569 to ~3583 cm^{-1}.

3. Results

3.1. Mineral abundance and morphology

The mineral assemblage of experimental charges consists of magnetite, clinopyroxene, plagioclase, and orthopyroxene, in order of appearance (Fig. 2). Magnetite and clinopyroxene cosaturate the melt as *liquidus* phases. However, the presence of tiny magnetite crystals on the *liquidus* is likely a consequence of the oxidizing conditions imposed during the experiments. Mineral phase relations and the crystallization

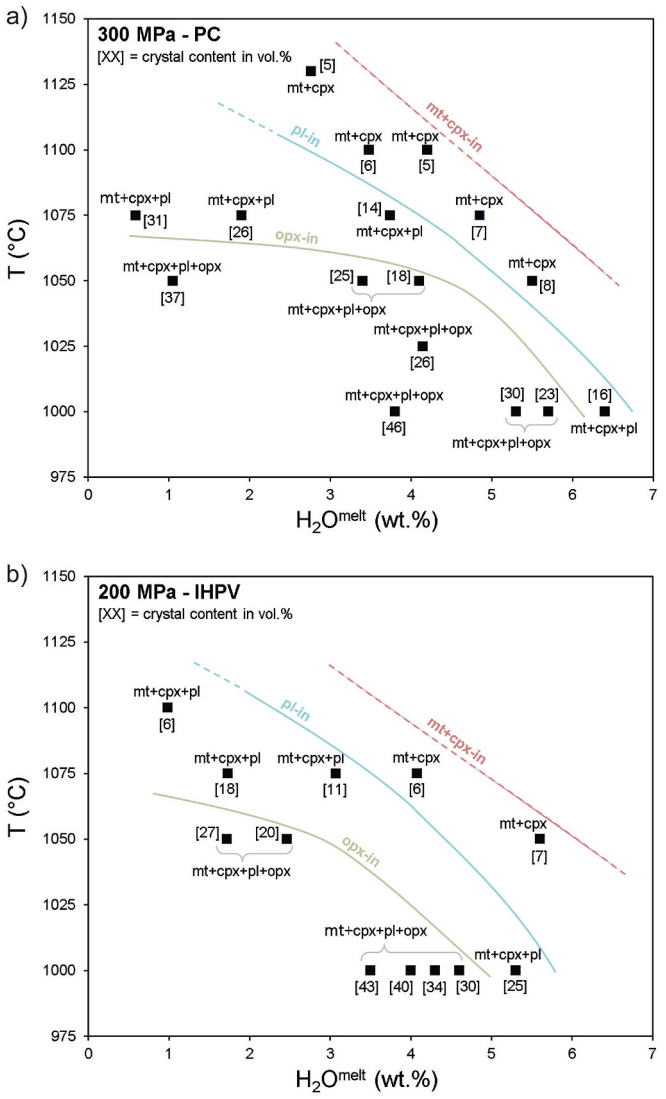

Fig. 2. Mineral phase relations in PC (a) and IHPV (b) experiments as a function of H_2O^{melt} and T. Mt.; magnetite. Cpx; clinopyroxene. Opx; orthopyroxene. Pl; plagioclase.

sequence in both PC (Fig. 2a) and IHPV (Fig. 2b) charges are consistent and comparable. The overall crystal content increases from ~5 to ~46 vol% as T and H_2O^{melt} decrease from 1130 to 1000 °C and from 6.4 to 0.6 wt%, respectively (Table 1 and Fig. 2). The only difference between the two sets of PC and IHPV experiments is the slight yet noticeable extension of plagioclase and orthopyroxene stability to temperatures ~15 °C higher in the 300 MPa PC charges compared to the 200 MPa IHPV charges. However, this shift in saturation temperature occurs when H_2O^{melt} exceeds 3 wt%, whereas it remains negligible at lower melt-water contents. At the same time, variations in fO_2 do not induce appreciable changes in the phase relations and/or modal proportions, as these are primary governed by T and H_2O^{melt} (Table 1), and most iron persists in the ferric state under the relatively oxidizing conditions of the experiments (Supplementary Material 1). The stability field of plagioclase expands significantly with decreasing T and/or H_2O^{melt} (Fig. 2), while a similar, though less pronounced, trend is observed for orthopyroxene. In highly crystallized charges obtained at T = 1000 °C, plagioclase becomes the most abundant mineral phase, accompanied by a sharp increase in magnetite modal abundance (Table 1). The volumetric ratio between plagioclase and clinopyroxene also abruptly shifts from ~0.3–0.8 at 1050–1075 °C to ~1.1–1.5 at 1000 °C, where feldspar crystallization is increasingly favored over the mafic mineral due to pronounced melt differentiation under lower thermal conditions.

Texturally, magnetite and clinopyroxene crystals typically grow as isolated mineral phases dispersed in abundant matrix glass at $T \geq$ 1100 °C (Fig. 3). Larger, prismatic clinopyroxene crystals with well-formed planar edges sometimes enclose smaller, sub-rounded titanomagnetite crystals. The maximum length (L_{max}) of magnetite and clinopyroxene crystals does not exceed ~20 and 50 μm, respectively. At $T \leq$ 1075 °C, tiny magnetite crystals occur within both poikilitic clinopyroxene and plagioclase (Fig. 3). As the crystal content increases, clinopyroxene growth is interrupted by the contiguous growth of tabular plagioclase (L_{max} = 100 μm), leading to the entrapment of small clinopyroxene grains within the feldspar. Intergrowth textures mainly develop in densely crystallized areas, when mutually touching clinopyroxene grains are embedded in plagioclase (Fig. 3). Orthopyroxene exhibits a euhedral morphology (L_{max} = 80 μm) and its growth is occasionally associated with the entrapment of small magnetite and clinopyroxene grains (Fig. 3).

BSE photomicrographs highlight that silicate minerals are unzoned across different crystallographic orientations, with no appreciable changes in the average atomic number of the crystalline regions (Fig. 3). The absence of zoning patterns pairs with the development of polyhedral forms in all the experimental charges (Fig. 3), suggesting complete textural maturation as the result of an interface-limited crystallization regime. This growth mechanism prevents morphological instability and the formation of skeletal or dendritic crystals.

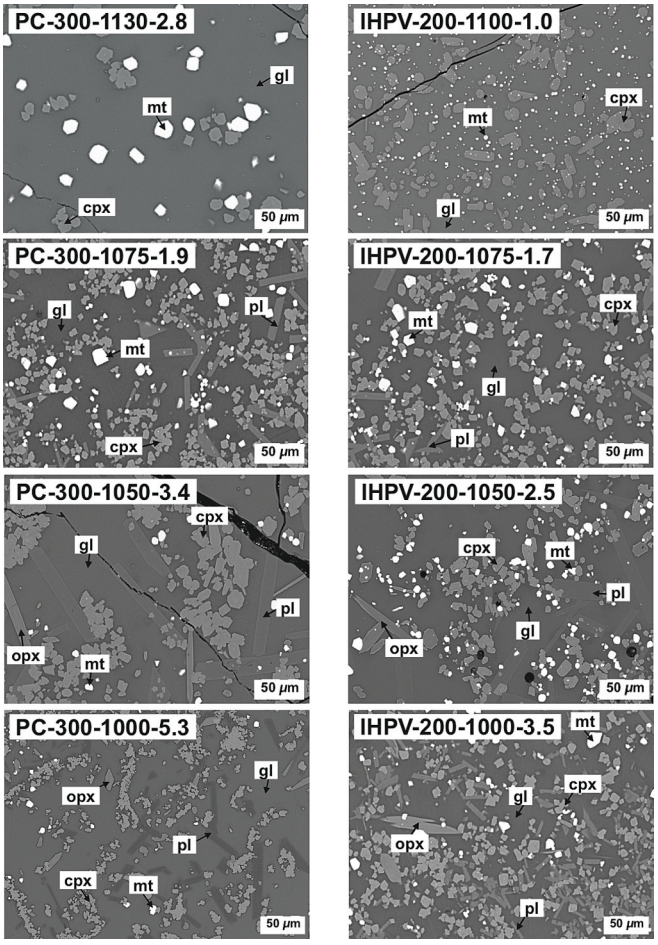

Fig. 3. Representative textural features of PC (left panels) and IHPV (right panels) experiments. Mt.; magnetite. Cpx; clinopyroxene. Opx; orthopyroxene. Pl; plagioclase. Gl; glass.

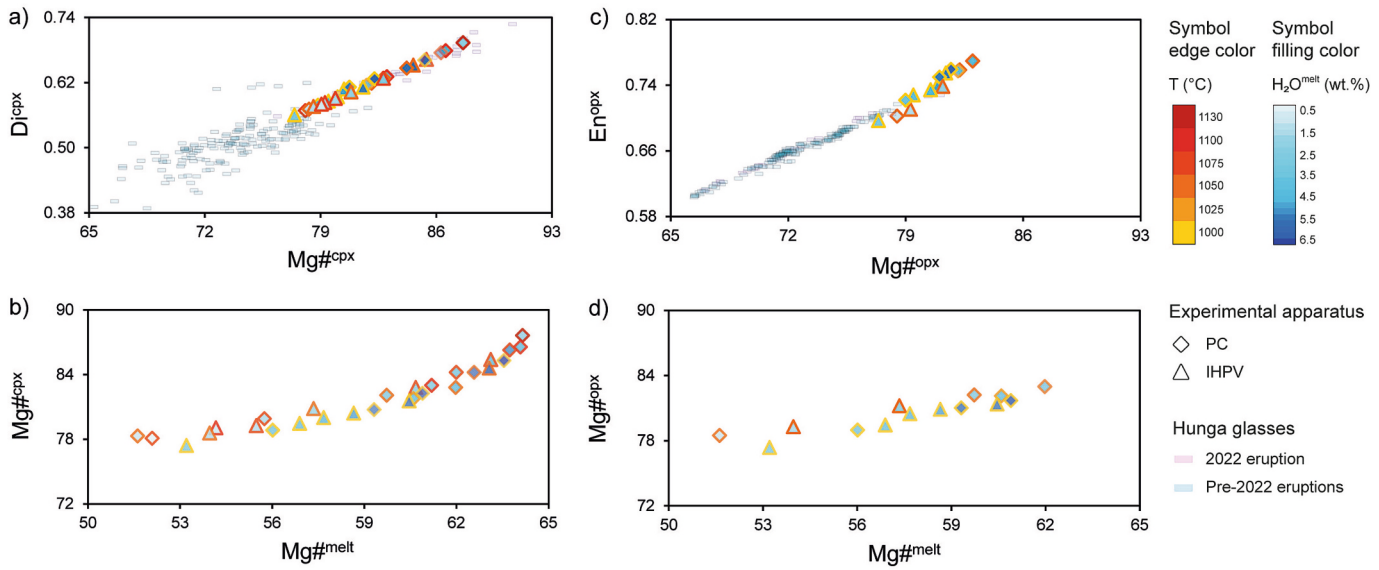

Fig. 4. Compositional variations of clinopyroxene and orthopyroxene crystals from PC and IHPV experiments. Mg# in clinopyroxene vs. diopside component (a). Mg# of the melt vs. Mg# in clinopyroxene (b). Mg# in orthopyroxene vs. enstatite component (c). Mg# of the melt vs. Mg# in orthopyroxene (d). For comparison, natural compositions of pyroxene phenocrysts from the pre-2022 and 2022 eruptions are also displayed. Chemical compositions of pre-2022 natural products are reported in Brenna et al. (2022), whereas those of the 2022 products are from Wu et al. (2025). Given the scale adopted in the figures, the error bars fall within the graphical resolution of the symbols and cannot be resolved visually.

3.2. Mineral chemistry

Electron microprobe chemical maps of representative PC and IHPV experiments (P = 200–300 MPa, T = 1000-1100 °C, and H_2O^{melt} = 1.7–4.6 wt%; Supplementary Material 1) confirm the absence of zoned crystals, as observed in BSE photomicrographs. The mineral compositions are homogeneous and stoichiometric within each experimental charge. When atoms per formula unit (apfu) are calculated for different mineral groups using standard normalization procedures, incorporating charge-balance assumptions and site assignments in the structural formula, the sum of cations never exceeds ±0.004 apfu (Supplementary Material 1). For the most complex pyroxene formula, apfu are calculated as reported in Morimoto (1988), with cations allocated in the order of site filling T, M1, then M2, and placed subsequentially as Si, Al, Fe^{3+}, Ti, Cr, Mg, Fe^{2+}, Mn, Ca, and Na. The sum of cations in the formula is adjusted to obtain occupancy [M1 + M2 + T] = 4.000 apfu, following the charge-balance criterion of Droop (1987). All mineral components are expressed in mole fractions.

Clinopyroxene from experimental charges is classified as augite (Morimoto, 1988). Di^{cpx} and $Mg\#^{cpx}$ vary sympathetically as a function of T and H_2O^{melt}, ranging from ~0.56 to ~0.69 and from ~77 to ~88, respectively, (Fig. 4a). Di^{cpx} represents the diopside component, while $Mg\#^{cpx}$ is determined from the crystal structural formula as [Mg / (Mg + Fe)] × 100, with divalent iron expressed hereafter as Fe instead of Fe^{2+} for convenience (see Discussion below). The effect of increasing H_2O^{melt} on clinopyroxene chemistry is analogous to the increase in T, as dissolved water lowers the *liquidus* temperature of the melt (Fig. 4a). Additionally, the compositional evolution of clinopyroxene crystals is well correlated with the degree of melt differentiation (Fig. 4b), expressed as $Mg\#^{melt}$ and calculated using divalent iron from the recent thermodynamic formalism of Sun and Yao (2024).

Orthopyroxene from experimental charges is classified as enstatite. The end-member component En^{opx} increases from ~0.70 to ~0.77 as both T and H_2O^{melt} gradually increase (Fig. 4c). The value of $Mg\#^{opx}$ ranges from ~77 to ~83 and its variation is positively correlated with En^{opx}. The evolutionary path of orthopyroxene aligns with the degree of melt differentiation, with $Mg\#^{opx}$ decreasing uniformly as $Mg\#^{melt}$ decreases (Fig. 4d).

Plagioclase from experimental charges is typically bytownite. The anorthite end-member component (An^{pl}, expressed in mole fraction) is more favorably incorporated into the lattice site of the crystals with increasing both T and H_2O^{melt}, ranging from ~0.70 to ~0.88 (Fig. 5a). An^{pl} gradually decreases with decreasing $Mg\#^{melt}$ (Fig. 5a). FeO^{pl} in plagioclase is also inversely correlated with An^{pl} (Fig. 5b).

The only oxide mineral identified in the experimental charges is magnetite, with total iron content FeO^{mt} varying from ~86 to ~90 wt%. $Mg\#^{mt}$ ranges from ~15 to ~26 (Fig. 6a), while $Cr\#^{mt}$, calculated as [Cr / (Cr + Al)] × 100, ranges from ~0.1 to ~0.5 (Fig. 6b). As observed for the other mineral phases, the chemistry of magnetite is also strongly influenced by the degree of melt differentiation, expressed as $Mg\#^{melt}$ (Fig. 6).

3.3. Glass chemistry

Within the analytical resolution of 2 μm pixel size, electron microprobe chemical maps document the achievement of a chemically homogeneous glass composition in both PC and IHPV experimental charges (Supplementary Material 1). Comparatively, 2D Raman mapping confirms the absence of water concentration gradients in the glass surrounding the crystals (Supplementary Material 1). Furthermore, the Raman spectra shows no evidence of nanostructuration in the glass (Supplementary Material 1). In particular, the diagnostic band near 670 cm^{-1} is absent (e.g., Di Genova et al., 2017), supporting the absence of devitrification phenomena upon heating from room temperature to the experimental target temperature. Because H^+ behaves as an incompatible element in nominally anhydrous minerals, the lack of an uphill water diffusion in proximity of the crystal surface indicates a slow advancement of the crystalline layers upon interface-limited growth regimes. It is concluded that the equilibration time was likely long enough to minimize chemical concentration gradients in the hydrous melt, leading to the development of near-equilibrium crystal-melt interface reactions. This is also supported by the close correspondence observed between the compositions of pyroxenes ($Mg\#^{cpx}$ and $Mg\#^{opx}$; Fig. 4b-d), plagioclase (An^{pl}; Fig. 5a), and magnetite ($Mg\#^{mt}$ and $Cr\#^{mt}$;

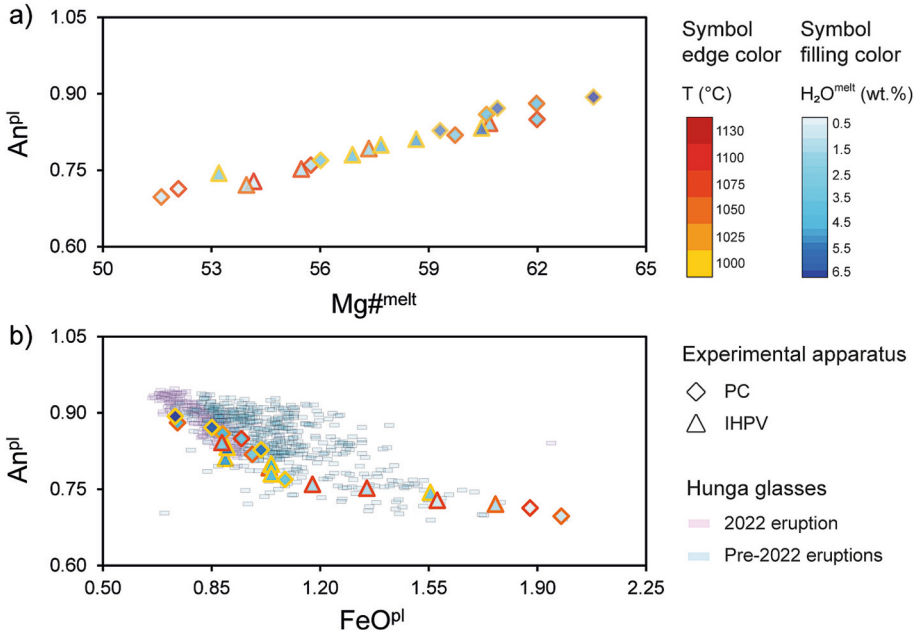

Fig. 5. Compositional variations of plagioclase crystals from PC and IHPV experiments. Mg# of the melt vs. anorthite component (a). FeO_{tot} in plagioclase vs. anorthite component (b). For comparison, natural compositions of plagioclase phenocrysts from the pre-2022 and 2022 eruptions are also displayed. Chemical compositions of pre-2022 natural products are reported in Brenna et al. (2022), whereas those of the 2022 products are from Wu et al. (2025). Given the scale adopted in the figures, the error bars fall within the graphical resolution of the symbols and cannot be resolved visually.

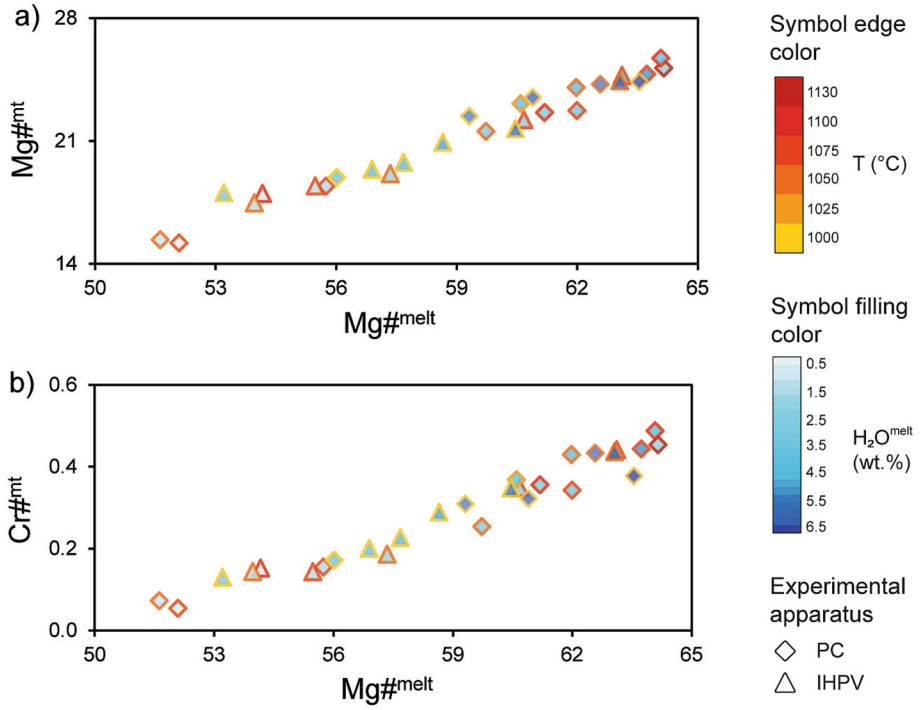

Fig. 6. Compositional variations of magnetite crystals from PC and IHPV experiments. Mg# of the melt vs. Mg# in magnetite (a). Mg# of the melt vs. Cr# in magnetite (b). Given the scale adopted in the figures, the error bars fall within the graphical resolution of the symbols and cannot be resolved visually.

Fig. 6) with that of the coexisting melt ($Mg\#^{melt}$), highlighting the absence of interlaboratory chemical variability and confirming the attainment of near-equilibrium crystallization conditions across both PC and IHPV experimental systems.

According to the TAS (total alkali vs. silica; Le Bas et al., 1986) classification diagram, experimental glasses exhibit compositions ranging from andesite to dacite, compared to the basaltic andesite starting material (Fig. 7a). As expected, residual glasses become more differentiated with decreasing T and H_2O^{melt}. However, two distinct sub-parallel trends are identified under high ($T > 1000$ °C) and low ($T = 1000$ °C) thermal conditions (Fig. 7a). At $T = 1000$ °C, the overall crystal content increases significantly up to 46 vol% (Table 1). As a result of pronounced crystallization, the residual melts evolve along a silica-rich dacitic trend (Fig. 7a), primarily driven by the enhanced stability of

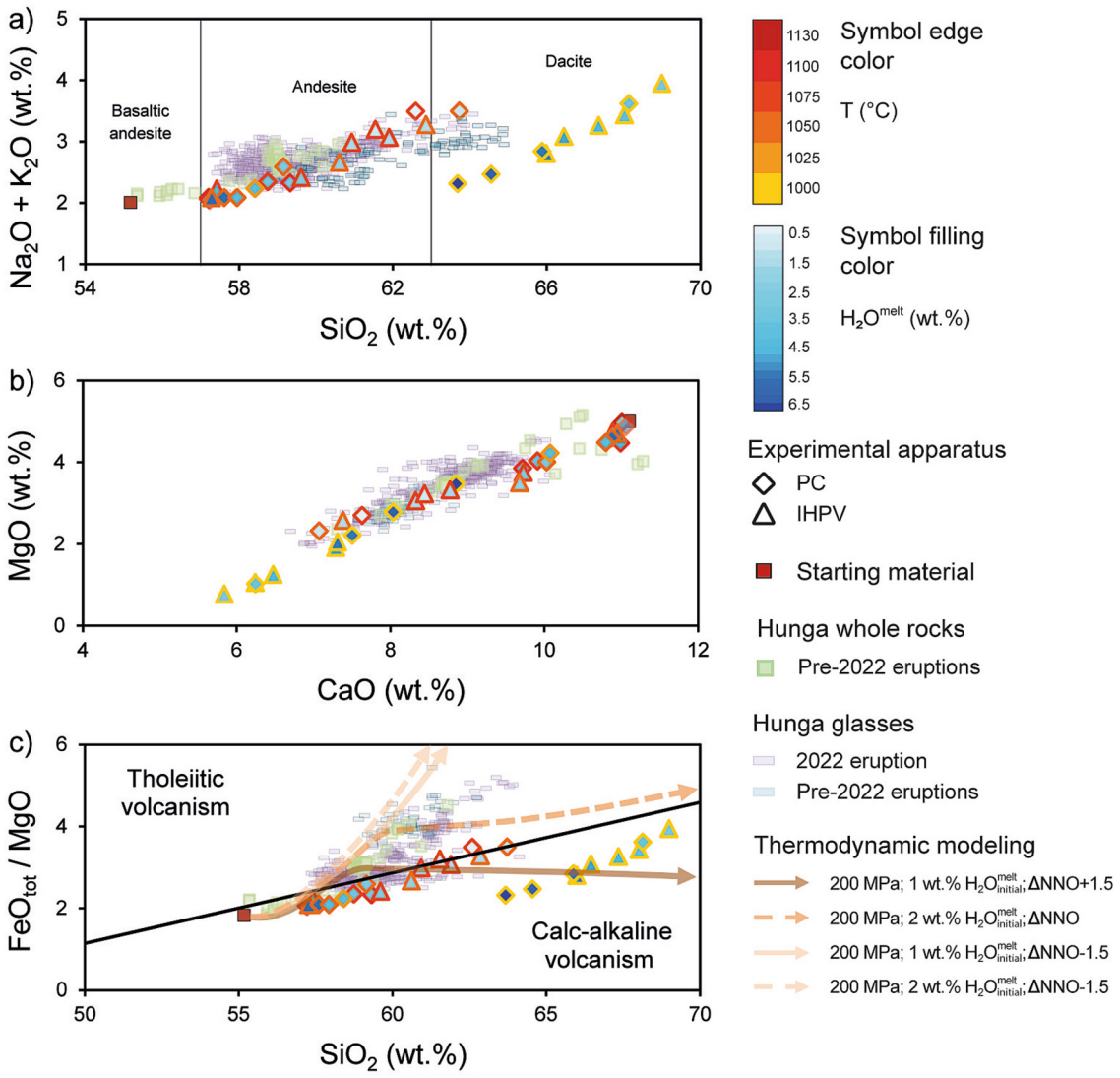

Fig. 7. Compositional variations of glasses from PC and IHPV experiments. TAS (total alkali vs. silica) classification diagram after Le Bas et al. (1986) (a). CaO vs. MgO diagram (b). FeO_{tot}/MgO vs. SiO_2 classification diagram after Miyashiro (1974) (c). Selected compositional trends obtained from thermodynamic simulations using the rhyolite-MELTS code (v.1.2.0; Gualda et al., 2012) are plotted in the diagram of Miyashiro (1974). The overall thermodynamic dataset is provided in Supplementary Material 3. For comparison, natural compositions of whole rocks and glasses from the pre-2022 and 2022 eruptions are also displayed. Chemical compositions of pre-2022 natural products are reported in Brenna et al. (2022), whereas those of the 2022 products are from Wu et al. (2025, 2026). Given the scale adopted in the figures, the error bars fall within the graphical resolution of the symbols and cannot be resolved visually.

magnetite, whose modal abundance increases from up to 6 vol% (Table 1). This leads to a concurrent decrease in the total iron content (FeO_{tot}) of the melt, from ~7–8 wt% at $T > 1000$ °C to ~6–4 wt% at $T = 1000$ °C (Supplementary Material 1). Under the lowest thermal condition, $Na_2O + K_2O$ exhibit a moderate increase from ~2 to ~4 wt% in the silica-rich dacitic melts (Fig. 7a).

In terms of CaO and MgO concentrations, less differentiated glasses (~11 wt% CaO and ~4–5 wt% MgO) typically form under conditions of $T = 1050$–1100 °C and $H_2O^{melt} \approx 4$–6 wt%, whereas highly differentiated melts (~6–7 wt% CaO and ~1–2 wt% MgO) are produced at $T = 1000$ °C and $H_2O^{melt} < 5$ wt% (Fig. 7b). Notably, all the experimental glasses define an almost uniform CaO-MgO trend (Fig. 7b), indicating that the evolutionary path of the melt is chiefly controlled by the cotectic crystallization of clinopyroxene and plagioclase, which conjointly deplete the residual melt in MgO and CaO.

Based on the FeO_{tot}/MgO vs. SiO_2 classification diagram proposed by Miyashiro (1974), who reappraised the early AFM ($Na_2O + K_2O$ vs. FeO_{tot} vs. MgO) diagram of Irvine and Baragar (1971) for volcanic rock series in island arcs and active continental margins, the experimental glasses produced at $T > 1000$ °C predominantly display a calc-alkaline affinity (Fig. 7c). A subset of glasses lies near the boundary between the tholeiitic and calc-alkaline series, with some compositions slightly extending into the tholeiitic field with increasing SiO_2. In contrast, all glasses produced at $T = 1000$ °C exhibit a distinctly calc-alkaline character and plot further from the compositional boundary separating the calc-alkaline and tholeiitic fields. This shift is less pronounced for MgO-poor glasses (i.e., glasses with higher FeO_{tot}/MgO ratios) obtained at $H_2O^{melt} < 4$ wt% (Fig. 7c).

4. Discussion

4.1. Clinopyroxene compositional evolution upon P-T-fO_2-H_2O^{melt} variations at Hunga volcano

Experimental results from this study document that the crystallization of clinopyroxene is significantly favored over plagioclase at high temperatures and elevated melt-water contents (Table 1 and Fig. 2). The evolutionary path of experimental crystals closely reproduces the

compositions of clinopyroxene phenocryst cores from both pre-2022 (~0.53–0.60 Di^{cpx} and ~77–81 $Mg\#^{cpx}$) and 2022 (~0.59–0.73 Di^{cpx} and ~80–90 $Mg\#^{cpx}$) eruptions (Fig. 4a). These phenocryst cores form two distinct compositional clusters, with the more evolved pre-2022 compositions that are better reproduced at $T \leq 1100$ °C and $H_2O^{melt} \approx$ 1–2 wt%. Conversely, the more primitive clinopyroxene signatures from 2022 eruptions reflect the injection of a mafic magma into the shallow reservoir (Yuen et al., 2022; Le Mevèl et al., 2023; Wu et al., 2025). In our experiments, the most magnesian-rich clinopyroxene with ~0.69 Di^{cpx} and ~88 $Mg\#^{cpx}$ readily saturates the basaltic andesitic melt at $T =$ 1130 °C and $H_2O^{melt} \approx 3$ wt% (Fig. 4a). Melt inclusions in clinopyroxene phenocrysts from the 2022 eruption yield a maximum melt-water content of ~3 wt% (Wu et al., 2025), which further constraints the saturation temperature of primitive crystal cores to ~1130 °C, given the compositional dependence of clinopyroxene on both T and H_2O^{melt} (Fig. 4a).

Equilibration of experimental crystals occurs at pressures of 200 and 300 MPa, corresponding to depths of 7–11 km, based on a representative crustal density estimate of ~2700 kg/m^3 for the Hunga volcano (Le Mevèl et al., 2023). Notably, these pressure conditions reflect the deeper segments of a more complex plumbing system, as revealed by geophysical data indicating the presence of three distinct low-density regions (Le Mevèl et al., 2023). Interpretation of marine gravity anomalies derived from satellite altimetry, before and after the 2022 eruptions, points to substantial magma accumulation in a multireservoir plumbing system extending from 2 to 10 km depths, with the larger, low-density body offset by 5 km to the north of the caldera and spanning depths of 3 to 10 km (Le Mevèl et al., 2023). Given this complexity, our isothermal-isobaric experiments do not capture the most evolved compositions of natural clinopyroxene phenocryst rims and groundmass crystals (~0.39–0.53 Di^{cpx} and ~65–76 $Mg\#^{cpx}$; Fig. 4a), which likely form at shallower crustal levels upon dynamic crystallization conditions driven primarily by magma ascent, decompression, and volatile exsolution (e.g., Mollo et al., 2015; Perinelli et al., 2016).

The pressure-sensitive jadeite ($NaAlSi_2O_6$) component in experimental clinopyroxene crystals does not exceeds ~0.01–0.02 Jd^{cpx}, regardless of a 100 MPa increase in the experimental equilibration pressure (Supplementary Material 1). Although the molar volume change of the fusion reaction $[NaAlSi_2O_6]^{melt} = [NaAlSi_2O_6]^{cpx}$ decreases with increasing P, the partitioning of Na (D_{Na}) between clinopyroxene and melt remains consistently low, yielding $D_{Na} < 0.1$ over a large pressure range from 1 atm to 3 GPa (Blundy et al., 1995). Within this pressure range, the clinopyroxene crystallochemistry yields a substantial pressure uncertainty of ±400 MPa in reproducing 1-bar values of enthalpy, entropy, and molar volume changes for jadeite crystallization, derived from calorimetric and partial molar volume measurements (Putirka et al., 2003). Therefore, polybaric crystallization at depths down to 10 km within the plumbing system of Hunga volcano exerts a negligible influence on the clinopyroxene chemistry compared to other intensive thermodynamic parameters, such as T and H_2O^{melt}.

The temperature-dependent Tschermak substitution [^{2T}Si, ^{M1}Mg] ↔ [^{2T}Al, ^{M1}Ti] (Putirka, 2008) is one of the main drivers for the decrease of diopside component in clinopyroxene during melt differentiation (Fig. 4a,b). The decrease of silica activity in the melt due to an increase of dissolved water also favors the substitution of aluminum for silicon in clinopyroxene (Dolfi and Trigila, 1983), further promoting incorporation of Tschermak components at the expense of diopside (Fig. 4a,b). The Fe^{2+}/Fe^{3+} ratio in experimental clinopyroxene crystals does not reliably reflect variations in fO_2 under our experiments (Supplementary Material 1), primarily because charge balance compensation mechanisms are dominated by Si-^{T}Al exchange in the lattice site, which is more strongly influenced by temperature and melt-water content than by oxygen fugacity (Putirka, 2016). Consistently, Toplis and Carroll (1995) document that the Fe–Mg exchange between clinopyroxene and melt, along with the Ca/Fe molar ratios in both phases, are independent of fO_2 in anhydrous ferrobasaltic systems. Likewise, Botcharnikov et al. (2008) highlight that the effect of redox conditions on clinopyroxene crystallochemistry cannot be isolated from the influence of water activity in hydrous ferrobasalts. While the determination of ferric iron in clinopyroxene by stoichiometry has been re-evaluated using Mössbauer spectroscopy (Neave et al., 2024), X-ray diffraction data indicate that Fe^{2+}/Fe^{3+} ratios estimated by electron microprobe analyses differ significantly from those obtained through crystal structure refinements (Tommasini et al., 2022). To reconcile these conflicting observations, as well as other controversial results from a broad spectrum of mineralogical and petrological studies (Rossman, 1980; McGuire et al., 1989; Canil and O'Neill, 1996; De Grave and Eeckhout, 2003; McCanta et al., 2004; Del Bello et al., 2014), we emphasize that the iron valence state in clinopyroxene is strongly influenced by crystallochemical effects involving multiple substitution reactions, such as [^{M1}Mg, ^{M2}Mg] ↔ [$^{M1}Fe^{2+}$, $^{M2}Fe^{2+}$], [^{M1}Al] ↔ [$^{M1}Fe^{3+}$], and [^{T}Si, ^{M1}Mg] ↔ [^{T}Al, $^{M1}Fe^{3+}$] (e.g., Mollo et al., 2018). This interpretation is consistent with thermodynamic parameterizations showing that the stability of $CaFe^{3+}AlSiO_6$ in clinopyroxene is inextricably interrelated to the thermodynamic properties of $CaMgSiO_2$-$CaAl_2SiO_6$-$CaTiAl_2O_6$ multicomponent reciprocal solutions (Sack and Carmichael, 1984; Sack and Ghiorso, 1994). It is also true that the amount of tetrahedrally coordinated ferrous cations in more oxidized melts is governed by the increasing number of aluminum cations in tetrahedral polyhedra and the charge balancing role of alkalis in the melt structure (Dickenson and Hess, 1986). On this basis, it is likely that any potential fO_2-related control on the Fe^{2+}/Fe^{3+} ratio in clinopyroxene is largely mitigated by the thermochemical evolution of the solidifying system under investigation (cf. Di Fiore et al., 2021).

4.2. Thermodynamic modeling of the Fe–Mg exchange between orthopyroxene and clinopyroxene

As outlined by our experimental data, orthopyroxene joins the mineral assemblage at $T \leq 1050$ °C and becomes markedly more stable at lower temperatures, even when the amount of H_2O^{melt} exceeds 5 wt% at $T = 1000$ °C (Fig. 2). The evolutionary trend depicted by the experimental crystals reproduces only the most mafic phenocrysts from both pre-2022 and 2022 eruptions (Fig. 4c). A slight deviation between experimental and natural En^{opx} contents is found at $Mg\#^{opx} \leq 71$ (Fig. 4c), likely due to subtle variations in temperature at the final stage of magma crystallization. According to this supposition, the compositions of orthopyroxene phenocrysts from pre-2022 and 2022 eruptions do not cluster in two distinct groups, as observed for clinopyroxene. Rather, they overlap within a similar range of ~0.60–0.73 En^{opx} (Fig. 4c), suggesting comparable low-temperature pathways for magmas before eruption.

To thermodynamically constrain the thermal evolution of magmas during the late stages of crystallization at Hunga volcano, the Fe–Mg exchange between orthopyroxene and clinopyroxene is evaluated by comparing $K_{D,Fe-Mg}^{opx-cpx}$ values from this study with those obtained from 295 phase equilibrium experiments reported in the EarthChem LEPR+ database (Supplementary Material 2). This database encompasses pressure and temperature ranges of ~0.001–30 kbar and ~1150–1780 K, thereby extending the orthopyroxene-clinopyroxene dataset (2–3 kbar and 1273–1323 K) from our study to a broader range of magmatic conditions. The plot of $\ln K_{Fe}^{opx-cpx}$ against $\ln K_{Mg}^{opx-cpx}$ is not perfectly linear (Fig. 8a), suggesting non-ideality in orthopyroxene and clinopyroxene solid solutions due to changes of interaction energies associated with cation intersite and intrasite mixing (e.g., Wood et al., 1980; Holland, 1983). As a result, the value of $K_{D,Fe-Mg}^{opx-cpx}$ is both influenced by temperature and the composition of solid solution, particularly the mole fraction of Ca (X_{Ca}) in clinopyroxene (Fig. 8b). This compositional control on the Fe–Mg exchange reflects the strong preference of Fe^{2+} for the M2 site and the constraint imposed by the partial occupancy of the M2 site by Ca (Blander, 1972; Kretz, 1981). The arithmetic mean for $K_{D,Fe-Mg}^{opx-cpx}$ varies

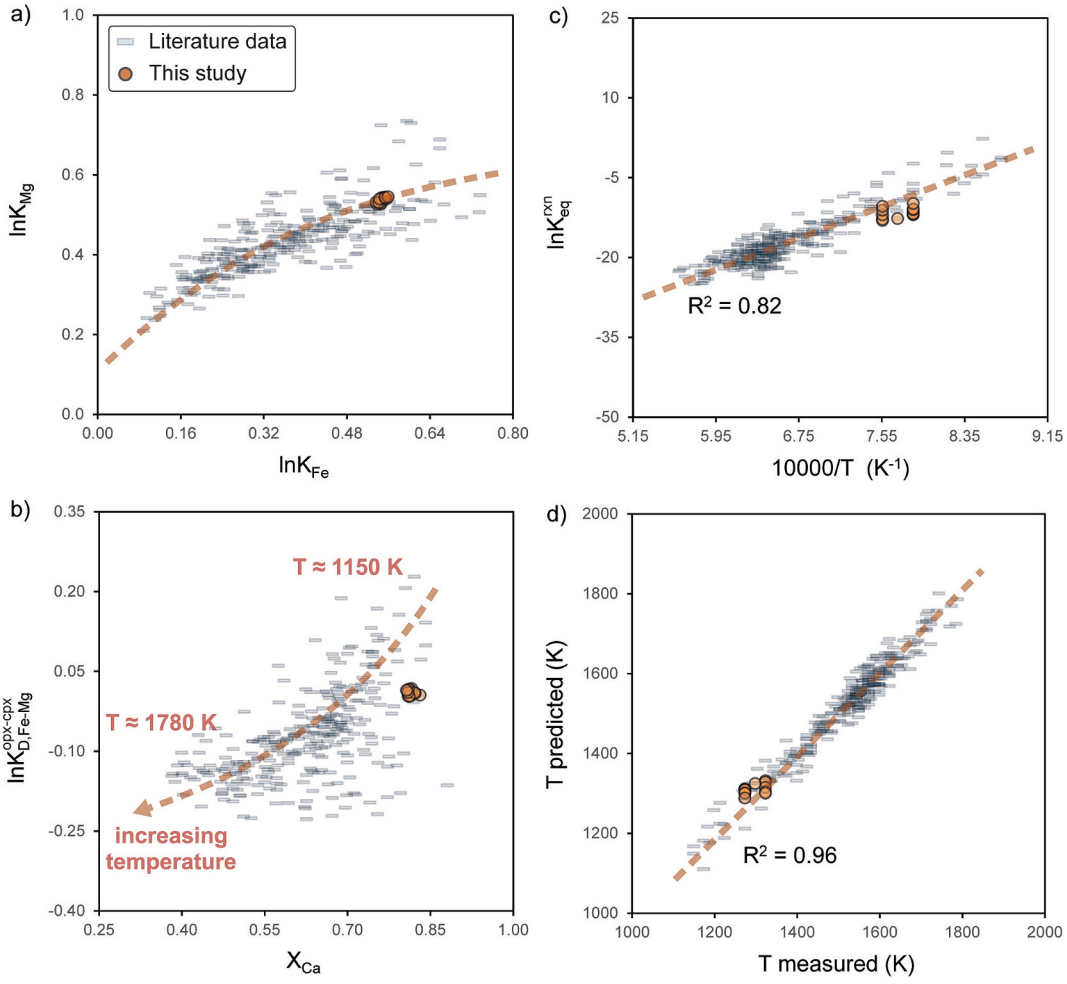

Fig. 8. Plot of $\ln K_{Fe}^{opx-cpx}$ against $\ln K_{Mg}^{opx-cpx}$ based on orthopyroxene and clinopyroxene cation fractions (a). Plot of X_{Ca} in clinopyroxene against $K_{D,Fe-Mg}^{opx-cpx}$ for the Fe–Mg exchange between orthopyroxene and clinopyroxene (b). Plot of $10000/T$ against $lnK_{eq}^{rxn\ (1)}$ for the Fe–Mg exchange between orthopyroxene and clinopyroxene evaluated in terms of macroscopic solution properties (c). Plot of T measured against T predicted by the two-pyroxene thermometer (d). The error propagation analysis based on crystal and melt compositions yields an uncertainty of ±11 °C for T, within the calibration error of the applied thermometer. Literature data are provided in Supplementary Material 3.

within a restricted interval of 0.94 ± 0.08 across the EarthChem LEPR+ database, which also includes orthopyroxene-clinopyroxene compositions from the present study, yielding an almost constant value of 1.01 ± 0.01. From a thermodynamic standpoint, this internal consistency between our and literature data supports the attainment of equilibrium crystallization conditions in our experiments and indicates that Fe–Mg exchange between orthopyroxene and clinopyroxene can be evaluated in terms of macroscopic solution properties of the reaction:

$$1/2Mg_2Si_2O_6{}^{opx}\ (En^{opx}) + CaFeSi_2O_6{}^{cpx}\ (Hd^{cpx}) = 1/2Fe_2Si_2O_6{}^{opx}\ (Fs^{opx}) + CaMgSi_2O_6{}^{cpx}\ (Di^{cpx}) \quad (1)$$

The chemical potential μ_i^j of each component i in the mineral phase j is:

$$\mu_i^j = \mu_i^{o,j} + RTlna_i^j \quad (2)$$

where $\mu_i^{0,j}$ is the standard chemical potential for each of the end-member component in its standard state. The macroscopic activity term in Eq. (2) is defined as $a_i^j = \gamma_i^j X_i^j$, where γ_i^j and X_i^j are the macroscopic activity coefficient and the thermodynamic mole fraction of end-member components (ideal mixing activities) in orthopyroxene and clinopyroxene. R is the ideal gas constant (8.314 J mol^{-1} K^{-1}) and T is the temperature in Kelvin of the system. According to the definition of chemical potential, the mass-balanced equilibrium exchange reaction (1) is defined as:

$$1/2\mu_{En}^{o,opx} + RTln(a_{En}^{opx})^{1/2} + \mu_{Hd}^{o,cpx} + RTln(a_{Hd}^{cpx}) = 1/2\mu_{Fs}^{o,opx} + RTln(a_{Fs}^{opx})^{1/2} + \mu_{Di}^{o,cpx} + RTln(a_{Di}^{cpx}) \quad (3)$$

The equilibrium constant $K_{eq}^{rxn\ (1)}$ can be reformulated using the macroscopic activity terms:

$$RTlnK_{eq}^{rxn\ (1)} = RTln\left[\frac{(a_{Fs}^{opx})^{1/2}(a_{Di}^{cpx})}{(a_{En}^{opx})^{1/2}(a_{Hd}^{cpx})}\right] \quad (4)$$

Consequently, the thermodynamic expression for orthopyroxene-clinopyroxene equilibrium becomes:

$$\Delta\mu^{rxn\ (1)} = 0 = \Delta\mu^{o,rxn\ (1)} + RTlnK_{eq}^{rxn\ (1)} \quad (5)$$

where $\Delta\mu^{o,rxn\ (1)}$ is equivalent to $\Delta G_{(P,T)}^{o,rxn\ (1)}$, which corresponds to the standard Gibbs free energy change arising from the difference between products and reactants in the exchange reaction (1) for each pure end-member component at the pressure and temperature of interest. By introducing the exchange partition coefficient (or apparent equilibrium constant)

$$K_D^{rxn\ (1)} = \frac{\left(X_{Fs}^{opx}\right)^{1/2}\left(X_{Di}^{cpx}\right)}{\left(X_{En}^{opx}\right)^{1/2}\left(X_{Hd}^{cpx}\right)}, \tag{6}$$

it follows that

$$\Delta G_{(P,T)}^{o,rxn\ (1)} = RTlnK_D^{rxn\ (1)} + RTln\left[\frac{\left(\gamma_{Fs}^{opx}\right)^{1/2}}{\left(\gamma_{En}^{opx}\right)^{1/2}}\right] - RTln\left[\frac{\left(\gamma_{Hd}^{cpx}\right)}{\left(\gamma_{Di}^{cpx}\right)}\right] \tag{7}$$

Eq. (7) can be split into an ideal contribution, involving $K_D^{rxn\ (1)}$, and non-ideal (or excess) contributions, involving the macroscopic activity coefficients γ_i^j for orthopyroxene and clinopyroxene end-member components.

Recalling that $\gamma_i^j = 1$ and $a_i^j = X_i^j$ for ideal solid mixing solutions, the thermodynamic mole fractions in Eq. (6) can be defined as:

$$X_{Fs}^{opx} = X_{Fe}^{opx,M1} X_{Fe}^{opx,M2}, \tag{8}$$

$$X_{En}^{opx} = X_{Mg}^{opx,M1} X_{Mg}^{opx,M2} \tag{9}$$

$$X_{Di}^{cpx} = X_{Mg}^{cpx,M1} \tag{10}$$

and

$$X_{Hd}^{cpx} = X_{Fe}^{cpx,M1} \tag{11}$$

An ideal mixing on each type of site is assumed for orthopyroxene. This requires that Fe and Mg are randomly distributed between the M1 and M2 sites of the structural unit, without local charge balance constraints: $X_{Fe}^{opx,M1}/X_{Mg}^{opx,M1} = X_{Fe}^{opx,M2}/X_{Mg}^{opx,M2} = X_{Fe}^{opx}/X_{Mg}^{opx}$ (Powell, 1978). Ideal solution relationships for mixing on two different types of sites in the formula unit represent also a filtering criteria for phase equilibrium experiments reported in the EarthChem LEPR+ database (i.e., $X_{Fe}^{opx,M1}$ and $X_{Fe}^{opx,M2} \neq 0$). In clinopyroxene, Ca exclusively occupies the M2 site, and a short-range charge-balance ordering is assumed for the distribution of Al and Si in the T site of clinopyroxene. While Fe–Mg mixing on the M1 site is completely random, Na in the M2 site preserves local charge balance for the incorporation of Al in the M1 site. This coupling reduces the configurational (mixing) entropy of the activity-composition relationships of the ideal solid solution, as the position of Na in the lattice is determined by the position of Al. Consequently, the total entropy of mixing of the solution arises solely from cation disorder on the M1 site (Wood and Fraser, 1976). However, silicate solid solutions deviate to some extents to ideality because the enthalpy of mixing is never exactly zero. Consequently, non-ideality need to be taken into account in thermodynamic calculations involving both orthopyroxene and clinopyroxene end-members, as described below.

The thermodynamic properties of end-member components are calculated using the thermochemical model of Helgeson et al. (1978), where the apparent standard molar Gibbs free energy of formation $\Delta G_{i,(P,T)}^{o,j}$ of a pure end-member component at a given pressure and temperature is expressed as:

$$\Delta G_{i,(P,T)}^{o,j} = \Delta G_{i,f}^{o,j} + \left(G_{i,(P,T)}^{o,j} + G_{i,(P_r,T_r)}^{o,j}\right) \tag{12}$$

The term $\Delta G_{i,f}^{o,j}$ designates the standard molar Gibbs free energy of formation of the mineral from its elements in their stable form at the reference pressure ($P_r = 1$ bar) and temperature ($T_r = 298.15$ K). The parenthetical term $\left(G_{i,(P,T)}^{o,j} + G_{i,(P_r,T_r)}^{o,j}\right)$ refers to the differences in the absolute standard Gibbs free energy ($G_i^{o,j}$) caused by changes in pressure ($P - P_r$) and temperature ($T - T_r$). Following this approach, Davidson and Lindsley (1989) formulated a set of $\Delta G_{i,f}^{o,j}$ equations for orthopyroxene and clinopyroxene end-member components, resulting in the expression:

$$\Delta G_{(PT)}^{o,rxn\ (1)} = 24778 - 26.12T - 0.61P \tag{13}$$

Eq. (13) was derived through multiple regression analysis of thermochemical data listed in Table 1 of Davidson and Lindsley (1989). Regression statistics are: $R^2 = 0.99$, $SE = 429$ J mol^{-1}, and $RMSE = 416$ J mol^{-1}, where R^2, SE, and $RMSE$ refer to the coefficient of determination, standard error, root mean squared error, respectively. The small pressure coefficient suggests that the exchange reaction is weakly affected by pressure variations, in accord with the early observations of Davidson and Lindsley (1989) and Perkins and Vielzeuf (1992).

The orthopyroxene solid solution is approximated as a disordered multisite solution (Fe, Mg)^{M2}(Fe, Mg)^{M1}Si$_2$O$_6$, in which Fe and Mg fractionate between the M1 and M2 sites. If these structural units remain distinct from one another even at the end-member compositions of En and Fs, then a reciprocal solution model can be used to describe the metathetical reaction involving four end-member components (Ganguly, 1982):

$$\begin{aligned}&\left(Fe^{M2}, Fe^{M1}\right)Si_2O_6 + \left(Mg^{M2}, Mg^{M1}\right)Si_2O_6\\ &= \left(Fe^{M2}, Mg^{M1}\right)Si_2O_6 + \left(Mg^{M2}, Fe^{M1}\right)Si_2O_6\end{aligned} \tag{14}$$

Notably, the interactions of cations in orthopyroxene are not energetically independent due to changes of the non-configurational Gibbs energy arising from non-ideal mixing of Fe and Mg on M1 and M2 sites (Sack, 1980). This non-ideality in orthopyroxene can be expressed by the following excess terms (Thompson Jr, 1969):

$$\begin{aligned}RTln\left(\gamma_{En}^{opx}\right) = {} & W^{opx,M1}\left(X_{Mg}^{opx,M1}\right)^2 + W^{opx,M2}\left(X_{Mg}^{opx,M2}\right)^2\\ & + \Delta G_x^{o,opx}\left(X_{Mg}^{opx,M1} X_{Mg}^{opx,M2}\right)\end{aligned} \tag{15}$$

and

$$RTln\left(\gamma_{Fs}^{opx}\right) = W^{opx,M1}\left(X_{Fe}^{opx,M1}\right)^2 + W^{opx,M2}\left(X_{Fe}^{opx,M2}\right)^2 + \Delta G_x^{o,opx}\left(X_{Fe}^{opx,M1} X_{Fe}^{opx,M2}\right) \tag{16}$$

where $W^{opx,M1}$ and $W^{opx,M2}$ are adjustable interaction terms analogous to Margules parameters used in symmetrical solutions for the description of a multisite mineral phase with random mixing of cations on each site (Thompson Jr, 1969; Saxena and Ghose, 1971). The interaction terms were determined through a stepwise least squares regression of orthopyroxene-clinopyroxene compositions from the present study combined with data from the EarthChem LEPR+ database. The fit to experimentally bracketed compositions was iteratively refined until convergence, yielding a mutually consistent set of regression constants and correspondingly small residuals (within ±65 J mol^{-1}) in the final least squares solution:

$$W^{opx,M1} = 16853 - 2064\frac{1000}{T} \tag{17}$$

and

$$W^{opx,M2} = 16869 - 1098\frac{1000}{T} \tag{18}$$

By assuming that short-range interactions between Fe and Mg cations on both the two sites are negligible, Saxena and Ghose (1971) documented a decrease of $W^{opx,M1}$ and $W^{opx,M2}$ as the temperature increases. This temperature dependence is consistent with the least squares analysis applied to our extended dataset to derive Eqs. (17) and (18), showing no significant deviations from ideal mixing on individual M sites due to Fe–Mg substitution (cf. Sack, 1980). However, the excess terms γ_{En}^{opx} and γ_{Fs}^{opx} not only reflect the energetic interactions of cations within the individual sites, but also incorporate the interactions between the two sites. To account for these additional effects, an interaction

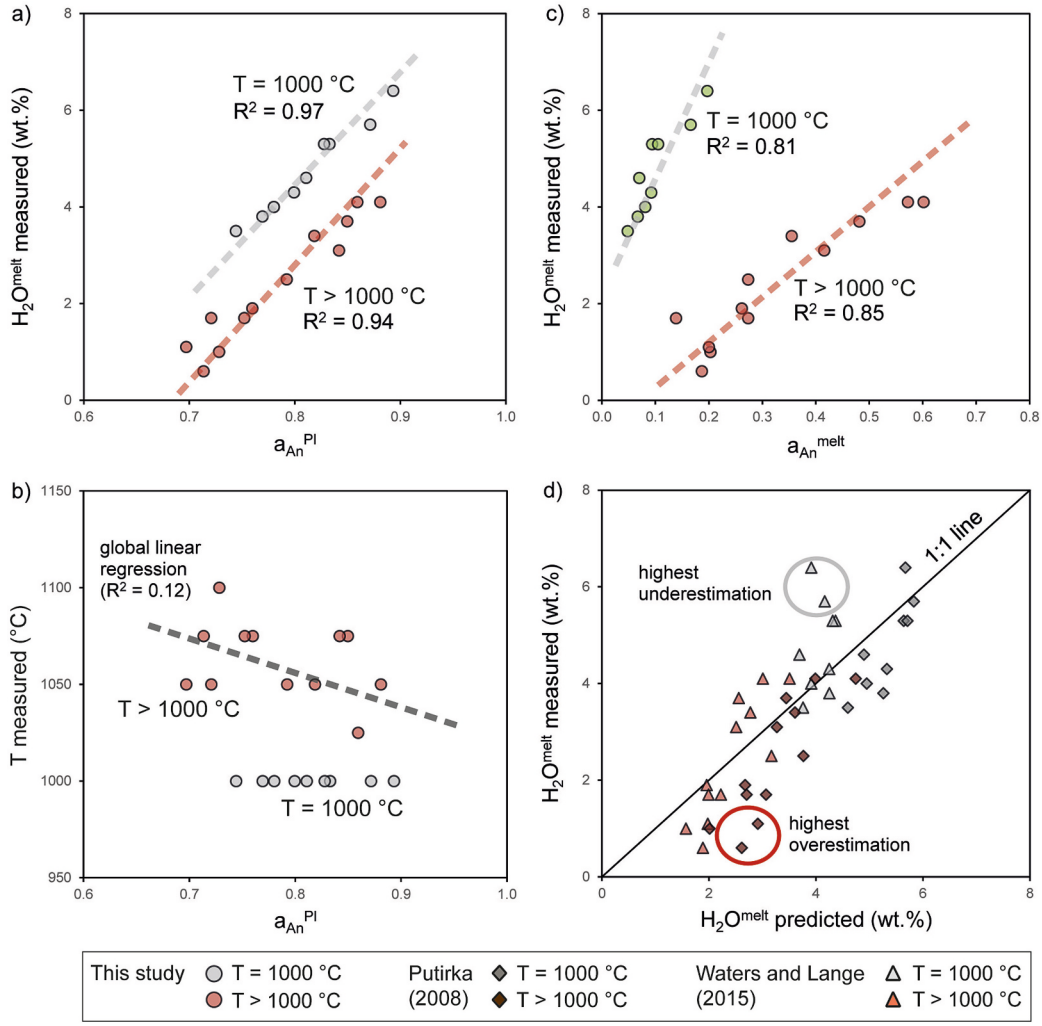

Fig. 9. Plot of a_{An}^{pl} against H_2O^{melt} (a) and T (b) measured in our experiments. Plot of a_{An}^{melt} against H_2O^{melt} measured in our experiments (c). Plot of H_2O^{melt} predicted by the models of Putirka (2008) and Waters and Lange (2015) against H_2O^{melt} measured in our experiments (d). The error propagation analysis based on crystal and melt compositions yields an uncertainty of ±0.33 wt% for H_2O^{melt}, within the calibration errors of the applied hygrometers.

parameter $\Delta G_x^{o,opx}$ is introduced into Eqs. (15) and (16), representing a Bragg-Williams type energy term for Fe–Mg ordering between M1 and M2 sites. The energy change associated with $\Delta G_x^{o,opx}$ results from the difference in standard molar Gibbs free energy between the ordered crystal and the crystal at its pure end-member compositions (Thompson Jr, 1969):

$$\Delta G_x^{o,opx} = 23941 + 455\frac{1000}{T} \tag{19}$$

This cross-term coefficient incorporates any compositional effect of a neighboring site on the ionic interaction within each site caused by the intracrystalline cation exchange reaction (Sack, 1980):

$$Fe^{M2} + Mg^{M1} = Mg^{M2} + Fe^{M1} \tag{20}$$

Consistent with the absence of a pressure term in Eq. (19), the intersite equilibrium constant $K_{D,Fe-Mg}^{opx,M1,M2}$ is largely insensitive to pressure variations because Fe–Mg intracrystalline fractionation is associated with very little volume changes in the solid solution (Ganguly and Saxena, 1987).

According to Powell and Powell (1974), clinopyroxene is modeled as a reduced three-component regular solution involving Fe, Mg, and Al^r, where $X_{Al^r}^{cpx,M1} = X_{Al}^{cpx,M1} + X_{Ti}^{cpx,M1} + X_{Cr}^{cpx,M1} + X_{Fe}^{cpx,M1}$. The excess mixing properties of diopside and hedenbergite in the lattice site are defined as:

$$\begin{aligned} RT\ln\left(\gamma_{Di}^{cpx}\right) = {} & W_{MgAl^r}^{cpx,M1}\left(X_{Al^r}^{cpx,M1}\right)^2 + W_{MgFe}^{cpx,M1}\left(X_{Fe}^{cpx,M1}\right)^2 \\ & + \left(X_{Fe}^{cpx,M1}X_{Al^r}^{cpx,M1}\right)\left(W_{MgFe}^{cpx,M1} + W_{MgAl^r}^{cpx,M1} - W_{FeAl^r}^{cpx,M1}\right) \\ & + W_{CaMg}^{cpx,M2}\left(X_{Wo}^{cpx,M2}\right) \end{aligned} \tag{21}$$

and

$$\begin{aligned} RT\ln\left(\gamma_{Hd}^{cpx}\right) = {} & W_{FeAl^r}^{cpx,M1}\left(X_{Al^r}^{cpx,M1}\right)^2 + W_{MgFe}^{cpx,M1}\left(X_{Mg}^{cpx,M1}\right)^2 \\ & + \left(X_{Mg}^{cpx,M1}X_{Al^r}^{cpx,M1}\right)\left(W_{MgFe}^{cpx,M1} + W_{FeAl^r}^{cpx,M1} - W_{MgAl^r}^{cpx,M1}\right) \\ & + W_{CaFe}^{cpx,M2}\left(X_{Wo}^{cpx,M2}\right) \end{aligned} \tag{22}$$

where $X_{Wo}^{cpx,M2} = \left(X_{Ca}^{cpx}\right)^2$ (cf. Lindsley et al., 1981), whereas the Margules parameters $W_{CaMg}^{cpx,M2}$ and $W_{CaFe}^{cpx,M2}$ represent the non-ideality of Ca–Mg and Ca–Fe mixing in clinopyroxene, respectively (Blander, 1972; Perkins and Vielzeuf, 1992). These interaction terms quantify deviations from ideal solution behavior due to the preference of Ca for the M2 site (Fig. 8b), which significantly influences the Fe and Mg fractionation between the M1 and M2 sites (Blander, 1972; Kretz, 1981). Using the least squares method on the extended dataset, the following values were determined: $W_{MgAl^r}^{cpx,M1} = 1287$, $W_{MgFe}^{cpx,M1} = 4466$, $W_{FeAl^r}^{cpx,M1} = 9939$, $W_{CaFe}^{cpx,M2} = 1118$, and $W_{CaMg}^{cpx,M2} = 9997$ J mol^{-1}.

Combining equations for ideal and non-ideal energetic contributions into Eq. (7) gives:

$$\begin{aligned}4777 - 26.12T - 0.61P = {} & RTlnK_D^{rxn\ (1)} + 1\Big/2\Big[W^{opx,M1}\left(X_{Fe}^{opx,M1}\right)^2 \\ & + W^{opx,M2}\left(X_{Fe}^{opx,M2}\right)^2 + \Delta G_x^{o,opx}\left(X_{Fe}^{opx,M1}X_{Fe}^{opx,M2}\right)\Big] \\ & - 1\Big/2\Big[W^{opx,M1}\left(X_{Mg}^{opx,M1}\right)^2 \\ & + W^{opx,M2}\left(X_{Mg}^{opx,M2}\right)^2 \\ & + \Delta G_x^{o,opx}\left(X_{Mg}^{opx,M1}X_{Mg}^{opx,M2}\right)\Big] + W_{MgAl^r}^{cpx,M1}\left(X_{Al^r}^{cpx,M1}\right)^2 \\ & + W_{MgFe}^{cpx,M1}\left(X_{Fe}^{cpx,M1}\right)^2 + \left(X_{Fe}^{cpx,M1}X_{Al^r}^{cpx,M1}\right)\left(W_{MgFe}^{cpx,M1}\right. \\ & \left. + W_{MgAl^r}^{cpx,M1} - W_{FeAl^r}^{cpx,M1}\right) + W_{CaMg}^{cpx,M2}\left(X_{Wo}^{cpx,M2}\right) \\ & - W_{FeAl^r}^{cpx,M1}\left(X_{Al^r}^{cpx,M1}\right)^2 - W_{MgFe}^{cpx,M1}\left(X_{Mg}^{cpx,M1}\right)^2 \\ & - \left(X_{Mg}^{cpx,M1}X_{Al^r}^{cpx,M1}\right)\left(W_{MgFe}^{cpx,M1} + W_{FeAl^r}^{cpx,M1}\right. \\ & \left. - W_{MgAl^r}^{cpx,M1}\right) - W_{CaFe}^{cpx,M2}\left(X_{Wo}^{cpx,M2}\right)\end{aligned} \tag{23}$$

The regression analysis of $lnK_{eq}^{rxn\ (1)}$ against $10000/T$ indicates a statistically significant linear dependence ($R^2 = 0.82$) between the equilibrium constant and temperature (Fig. 8c). Eq. (23) can be used to estimate temperatures of orthopyroxene-clinopyroxene pairs by rearranging the expressions for thermodynamic equilibrium and solving for temperature. After performing some algebraic manipulations and simplifications, we obtain:

$$\begin{aligned}\frac{10000}{T} = {} & \Big[-0.45\left(X_{Fe}^{opx,M1}\right)^2 + 27.30\left(X_{Fe}^{opx,M2}\right)^2 - 14.58\left(X_{Fe}^{opx,M1}X_{Fe}^{opx,M2}\right) \\ & + 11.88\left(X_{Mg}^{opx,M1}\right)^2 + 10.93\left(X_{Mg}^{opx,M2}\right)^2 - 23.83\left(X_{Mg}^{opx,M1}X_{Mg}^{opx,M2}\right) \\ & - 5.61\left(X_{Al^r}^{cpx,M1}\right)^2 + 3.88\left(X_{Fe}^{cpx,M1}\right)^2 - 0.88\left(X_{Fe}^{cpx,M1}X_{Al^r}^{cpx,M1}\right) \\ & + 1.77\left(X_{Wo}^{cpx,M2}\right) - 0.90\left(X_{Mg}^{cpx,M1}\right)^2 + 1.37\left(X_{Mg}^{cpx,M1}X_{Al^r}^{cpx,M1}\right) \\ & - 1.94\left(10^{-5}\right)(P) + 7.12\Big]\Big/\Big[0.99 + 0.02lnK_D^{rxn\ (1)} \\ & + 0.11\left(X_{Fe}^{opx,M1}\right)^2 + 0.01\left(X_{Fe}^{opx,M2}\right)^2 + 0.05\left(X_{Fe}^{opx,M1}X_{Fe}^{opx,M2}\right) \\ & + 0.02\left(X_{Mg}^{opx,M1}\right)^2 - 0.04\left(X_{Mg}^{opx,M2}\right)^2 - 0.07\left(X_{Mg}^{opx,M1}X_{Mg}^{opx,M2}\right)\Big]\end{aligned} \tag{24}$$

An algorithm based on Eq. (24), which can be readily applied to estimate the cosaturation temperature of natural orthopyroxene and clinopyroxene phenocrysts, is provided in Supplementary Material 2. Testing Eq. (24) on the extended dataset yields $RMSE = 26$ K, while linear regression of measured against estimated temperatures gives $R^2 = 0.96$ and $SE = 27$ K (Fig. 8d). When only orthopyroxene-clinopyroxene compositions from the present study are considered as an independent validation dataset, comparable regression statistics are obtained ($RMSE$ and $SE = 18$ K). Given the small pressure coefficient in Eq. (13), the influence of pressure on the temperature estimate is negligible at $P \leq 500$ MPa. Replacing the true calibration pressure with fictive pressures of 0.1 or 500 MPa increases the model error by only 4 K. In contrast, substituting a fictive pressure of 1 GPa leads to a markedly larger increase in model error (23 K). This error is comparable to, and generally lower than, those reported for thermometers based on orthopyroxene-melt (error of ±26–48 K) and clinopyroxene-melt (error of ±25–95 K) equilibria (see, for example, the review by Putirka, 2008). For a crustal pressure range between 1000 and 10000 bar, the temperature estimate increases slightly by ~20 K but remains within our model error, as the equilibrium constant of orthopyroxene-clinopyroxene exchange is predominantly dependent on temperature (Fig. 8c).

The two-pyroxene thermometer applies exclusively to magmas in which orthopyroxene crystallizes cotectically with clinopyroxene. Despite this limitation, the key advantage of the model lies in its independence from melt composition and from the compositional variations of residual melts due to the crystallization of matrix minerals at both syn- and post-eruptive stages. Moreover, since the calibration approach is based on purely thermodynamic grounds, the orthopyroxene-clinopyroxene thermometer ensures reliable extrapolations of the experimental determinations across broad *P-T-X* ranges (Newton and Haselton, 1981). Thermodynamic cation fractions and Margules parameters in Eq. (24) are the energetic expression of intersite and intrasite cation mixing, as well as substitutional order-disorder in orthopyroxene and clinopyroxene. In contrast, empirical models may be strongly influenced by the variance of the calibration dataset and the degree of multicollinearity in a set of multiple linear regression variables (e.g., Masotta et al., 2013; Mollo et al., 2015).

Application of the orthopyroxene-clinopyroxene thermometer to pre-2022 and 2022 eruptions at Hunga volcano indicates that orthopyroxene-clinopyroxene cosaturation occurred within comparable thermal ranges of 922–1048 °C (average temperature of 982 ± 42 °C) and 919–1051 °C (average temperature of 970 °C ± 34 °C), respectively. These thermal ranges satisfy the equilibrium selection criteria for natural pyroxene compositions, as defined by $K_{D,Fe-Mg}^{opx-cpx}$ values of 0.94 ± 0.08 derived above. These relatively low-temperatures reinforce the idea that most of the crystallization of orthopyroxene within the plumbing system of Hunga volcano is temporally and spatially related to a late-stage process when magmas are stored in shallow crustal reservoirs (Brenna et al., 2022). Both pre-2022 and 2022 volcanic products exhibit a mineral assemblage dominated by clinopyroxene and plagioclase, with minor amounts of orthopyroxene, typically comprising less than 3 vol%. However, as outlined by Grove and Baker (1984), orthopyroxene crystallization under low-temperature conditions may expand the stability of plagioclase over clinopyroxene (Table 1 and Fig. 2), thereby driving the residual melts from basaltic andesitic toward andesitic compositions (Fig. 7).

4.3. Plagioclase anorthite-albite solid solution: a proxy for temperature or melt-water content variations?

Experimental phase relations indicate that most plagioclase crystallization occurs under pseudounivariant cotectic conditions at $T \leq 1075$ °C and $H_2O^{melt} < 4$ wt% (Fig. 2). The crystal aspect ratios (length/width < 10) fall within the range expected for equilibrium crystallization conditions (Moschini et al., 2023), thereby excluding any influence of kinetic effects on plagioclase growth. Pressure has only a modest effect on mineral proportions, marginally expanding the stability fields of plagioclase and orthopyroxene at a rate of ~15 °C/100 MPa when H_2O^{melt} exceeds ~3 wt% (Fig. 2). Given the consistent mineral proportions and compositions observed at 200 and 300 MPa, we propose that our findings may extend to pressures as low as 100 MPa, with the crystallization path likely remaining similar under shallow crustal conditions.

Both experimental melt and crystal compositions (Fig. 5a,b) follow a single evolutionary trend, reflecting the strong interdependence of the bulk system on both T and H_2O^{melt}. Comparison with natural data reveals that the variability of 2022 plagioclase phenocrysts is restricted to calcic compositions (~0.81 to ~0.94 An^{pl}), while pre-2022 plagioclase phenocrysts extend to more sodic compositions (~0.70 to ~0.94 An^{pl}), with a wider range of FeO^{pl} values (Fig. 5b). The most anorthitic plagioclase phenocrysts (~0.90–0.94 An^{pl}) are not reproduced in our experiments, likely due to the early crystallization of magnetite on the *liquidus*. This promotes the formation of Mg- and Ca-rich clinopyroxene, thereby limiting the crystallization of plagioclase with $An^{pl} > 0.90$ (Blatter et al., 2013). Accordingly, our experiments constrain a minimum saturation

temperature of ~1075 °C at ~3 wt% H_2O^{melt} (Fig. 5a,b) for calcic plagioclase compositions at Hunga volcano. The increase in FeO^{pl} during plagioclase compositional evolution can be attributed either to the primarily control of melt redox state on iron speciation (Wilke and Behrens, 1999) or the preferential incorporation of iron into the lattice site as temperature decreases (Aigner-Torres et al., 2007). However, within our dataset, the increase of FeO^{pl} is tightly correlated with the decrease of An^{pl} (Fig. 5b), and no clear correlation is observed between iron in plagioclase and the oxygen fugacity imposed during the experiments (Supplementary Material 1). As reported in Toplis and Carroll (1995), plagioclase crystals in equilibrium with basaltic to dacitic melts at $T <$ 1100 °C do not exhibit any systematic relation between FeO^{pl} and fO_2, within a melt redox state variable from ΔNNO-1.3 to ΔNNO+1.7. Moreover, under the oxidizing crystallization conditions employed in our experiments, most of the total iron in the melt remains in the ferrous state, thus promoting the formation of $CaFeAlSi_2O_8$ component in plagioclase at the expense of $CaAl_2Si_2O_8$ (Moschini et al., 2023). Based on this exchange, subtle FeO^{pl} enrichments in natural phenocrysts from Hunga eruptions may reflect chemical and physical perturbations in a dynamic magmatic system. In this context, recurrent fluctuations in T and H_2O^{melt}, driven by convective magma mixing at shallow crustal levels (Brenna et al., 2022), can enhance the incorporation of iron into the lattice site of plagioclase under kinetically controlled crystallization conditions (Mollo et al., 2011, 2024).

The stability and composition of plagioclase are widely recognized in the literature to be predominantly controlled by temperature and the influence of water dissolved in the melt on the *liquidus* depression of feldspar (Glazner, 1984; Sisson and Grove, 1993; Putirka, 2005, 2008; Lange et al., 2009; Namur et al., 2012; Waters and Lange, 2015). Distinguishing between these two different contributions when applying plagioclase-based thermometers and hygrometers to natural magmatic systems is challenging and can lead to significant overestimations or underestimations, depending on the *P-T-X* state of magma (Mollo et al., 2011; Humphreys et al., 2016; Moschini et al., 2023). Predictive models for T and H_2O^{melt} rely on the An-Ab exchange reaction between plagioclase and melt:

$$CaAl_2Si_2O_8^{pl}\left(An^{pl}\right) + NaAlSi_3O_8^{melt}\left(Ab^{melt}\right) = CaAl_2Si_2O_8^{melt}\left(An^{melt}\right) + NaAlSi_3O_8^{pl}\left(Ab^{pl}\right) \quad (25)$$

From a thermodynamic perspective, Eq. (25) can be reformulated as:

$$\Delta G^{o,rxn\ (25)}_{(P,T)} = RT\ln K^{rxn\ (25)}_{eq} = RT\ln\left(\frac{a^{pl}_{An}}{a^{pl}_{Ab}}\right) - RT\ln\left(\frac{a^{melt}_{An}}{a^{melt}_{Ab}}\right) \quad (26)$$

At magmatic temperatures, the formation of An-Ab ordered domains implies that plagioclase end-member components behave nearly ideally due to the independence of vibrational states on geometric configurations (Glazner, 1984; Namur et al., 2012). Therefore, $a^{pl}_{An} \cong \left(X^{pl}_{An}\right)^{ideal}$ and $a^{pl}_{Ab} \cong \left(X^{pl}_{Ab}\right)^{ideal}$, as Al–Si mixing on the T-site with formation of Al-O-Al linkages does not contribute to the free energy of the An-Ab solid solution either enthalpically or entropically (Mollo et al., 2024).

For the melt counterpart, a^{melt}_{An} and a^{melt}_{Ab} can be approximated for the Hunga magmas using the polynomial expressions of Glazner (1984), which resemble a Margules power-series expansion for the excess free energy. These expressions were derived for plagioclase-melt experiments encompassing calc-alkaline compositions and extending up to dacitic melts (~64 wt% SiO_2). By interpolating various thermochemical data from the literature, Moschini et al. (2023) has also found that $\Delta G^{o,rxn(25)}_{(T)} >> \Delta G^{o,rxn(25)}_{(P)}$ and $\Delta G^{o,rxn(25)}_{(P,T)} \approx \Delta G^{o,rxn(25)}_{(T)}$ under crustal conditions. The lack of a clear influence of pressure on plagioclase compositions from our experiments confirms that the An-Ab exchange is mainly controlled by T and H_2O^{melt} variations during magma crystallization (Fig. 5a).

According to the above considerations, Fig. 9a shows a tight linear correlation between a^{pl}_{An} and H_2O^{melt} in both experimental subsets obtained at T = 1000 °C (R^2 = 0.97) and $T >$ 1000 °C (R^2 = 0.94). In contrast, no clear linear relationship is displayed in Fig. 9b between a^{pl}_{An} and T, as pointed out by the statistically insignificant linear regression (R^2 = 0.12) of the overall dataset. Consequently, the solution of anorthite in the growing plagioclase at Hunga volcano is mainly determined by the degassing path of magma (i.e., P_{H_2O}), with only a limited influence of temperature (e.g., Sisson and Grove, 1993; Moore and Carmichael, 1998). When a^{melt}_{An} is plotted against H_2O^{melt}, two sub-parallel trends are invariably depicted in Fig. 9c for the experimental subsets conducted at T = 1000 °C (R^2 = 0.81) and $T >$ 1000 °C (R^2 = 0.85). This indicates a comparable influence of the melt composition on water dissolution, accounting for the different crystallizing phase proportions of clinopyroxene and plagioclase. As a result, the melt and plagioclase activities do not vary independently as a function of dissolved water, which lowers the *liquidus-solidus* loop in the An-Ab system by expanding the stability of the calcic end-member relative to the sodic end-member. Moreover, the depolymerizing effect of water favors the proportion of octahedral relative to tetrahedral sites in the melt structure. An increased availability of non-bridging oxygens to form cation-oxygen polyhedra in the silicate framework aligns with the preferential role of hydroxyl groups in reducing the activity of $NaAlSi_3O_8$ relative to $CaAl_2Si_2O_8$ in the melt. Si-OH groups form more readily than Al-OH groups in hydrous magmatic melts, thereby reducing the activity of $NaAlSi_3O_8$ as the plagioclase component containing a greater proportion of SiO_2 compared to $CaAl_2Si_2O_8$ (Lange et al., 2009).

To correctly determine the amount of water in equilibrium with plagioclase crystals from Hunga magmas, the performance of plagioclase-based hygrometers from Putirka (2005) (M_{2005}; calibration error ± 1.1 wt% H_2O^{melt}), Putirka (2008) (M_{2008}; calibration error ± 1.1 wt% H_2O^{melt}), Lange et al. (2009) (M_{2009}; calibration error ± 0.32 wt% H_2O^{melt}), and Waters and Lange (2015) (M_{2015}; calibration error ± 0.35 wt% H_2O^{melt}) has been tested against our experimental dataset. The statistical analysis yields *RMSE* of 2.7, 1.0, 1.1, and 0.9 wt% for M_{2005}, M_{2008}, M_{2009}, and M_{2015}, respectively. The standard deviation σ of the difference between measured and predicted H_2O^{melt} values is 0.9, 0.6, 0.7, and 0.6 wt% for M_{2005}, M_{2008}, M_{2009}, and M_{2015}, respectively. Overall, the performance of hygrometers is very good, except for the early empirical model M_{2005} of Putirka (2005). The most recent semi-empirical model M_{2015} of Waters and Lange (2015), which relies on thermodynamic principles, provides the most accurate predictions (Fig. 9d). M_{2008} is also suitable for application to Hunga magmas, returning *RMSE* and σ very close to those determined using the model M_{2015} (Fig. 9d). However, due to the markedly different calibration strategies of the two hygrometers, M_{2015} underestimates water concentrations above ~5.5 wt% by ~2 wt%, whereas M_{2008} overestimates water concentrations below ~1.0 wt% by a similar extent (Fig. 9d). To assess the sensitivity of hygrometric predictions to temperature, we keep constant the plagioclase and melt compositions as input data for the models, while varying the experimental temperature by ±50 °C. The recalculated *RMSE* values for H_2O^{melt} are 2.7, 1.4, 1.3, and 1.2 wt% for M_{2005}, M_{2008}, M_{2009}, and M_{2015}, respectively, indicating minimal (0.2–0.4 wt%) or no changes compared to testing models against the actual experimental temperatures. This simple test confirms that most of the variance in the dataset is controlled by the amount of water dissolved in the melt at Hunga volcano, while the influence of temperature on hygrometric predictions remains almost negligible.

For the application of M_{2015} to natural products, we use plagioclase phenocryst cores from pre-2022 (~0.82–0.95 An^{pl}) and 2022 (~0.80–0.95 An^{pl}) eruptions as input data. These calcic crystal cores are paired with the less differentiated andesitic glasses analyzed in the volcanic products, which exhibit average compositions of ~59.0 wt% SiO_2 and ~2.5 wt% $Na_2O + K_2O$ for pre-2022 glasses, and ~58.5 wt%

SiO_2 and ~2.7 wt% $Na_2O + K_2O$ for 2022 glasses. Experiments from this study supports the legitimacy of this comparison, with plagioclase reaching cosaturation when the residual melt differentiates toward andesitic compositions. The attainment of equilibrium was also evaluated using the general model calibrated by Namur et al. (2012) to predict An^{pl} from cationic melt components normalized on an 8-oxygen basis. According to the authors, the difference between measured and predicted anorthite contents should not exceeds ±0.02. Plagioclase crystal rims are excluded from this modeling approach because their more evolved compositions (~0.70–0.84 An^{pl}) likely reflect syn-eruptive crystallization under dynamic growth regimes, which may introduce substantial uncertainty in H_2O^{melt} estimates. In line with this, magma decompression significantly lowers the original concentration of water dissolved in the melt, promoting the rapid overgrowth of anorthite-poor crystal rims, where cations are incorporated into the lattice site at disequilibrium proportions (e.g., Mollo et al., 2011, 2024; Humphreys et al., 2016). Considering the broad spectrum of An^{pl} in natural phenocryst cores, a conservative T of 1050 °C is adopted for the calculations. Sensitivity tests indicate that increasing the temperature to 1100 °C introduces an uncertainty of only ±0.3 wt% in the predicted H_2O^{melt} contents. Given the increasing crystal content of the melt and its consequent compositional evolution, it is highly improbable that calcic plagioclase cores equilibrated with the Hunga magmas under significantly lower thermal conditions. Results from calculations yield an average H_2O^{melt} of 2.6 ± 0.4 wt% and 2.8 ± 0.1 wt% for pre-2022 and 2022 eruptions, respectively. Notably, this range of dissolved water closely matches most melt inclusion data from plagioclase crystals in 2022 eruptions (Wu et al., 2025). Only a restricted subset of melt inclusion data extends to $H_2O^{melt} > 3$ wt%. According to Wu et al. (2025), this excess of water reflects abundant fractional crystallization of a nominally anhydrous mineral assemblage at Hunga volcano, resulting in sporadic melt inclusions in plagioclase that correspond to highly silicic andesites.

Based on the melt compositions used for the modeling and assuming $P_{tot} = P_{H_2O}$ at the time of eruptions, our estimates yield a water saturation pressure of 84 ± 12 MPa (i.e., 3.2 ± 0.5 km for an average crustal density of 2700 kg m^{-3}), as calculated through the thermodynamic solubility equation of Duan (2014). This estimated saturation pressure represents a conservative value compared to the 53–74 MPa range derived for matrix glasses from 2022 eruptions at Hunga volcano, which exhibit relatively high H_2O^{melt} contents (2.4–3.0 wt%) and are interpreted to reflect the upper levels of a shallow, stable pre-eruptive magma reservoir (Wu et al., 2025). More degassed matrix glasses (H_2O^{melt} = 0.7–1.5 wt%) are also present in the same eruptive products, indicating lower water saturation pressures (6–23 MPa) and minimum fragmentation/quenching depths of 0.4–1.0 km at the syn-eruptive stage (Wu et al., 2025). Within this lower melt-water range, our experiments reproduce plagioclase crystals with compositions of 0.70–0.73 An^{pl}, consistent with a decrease of anorthite content during groundmass crystallization due to magma ascent and volatile exsolution at the syn-eruptive stage.

4.4. Reconstruction of melt differentiation processes

Compared to the natural magmas at Hunga volcano, less differentiated glasses in our experiments closely match the SiO_2 concentrations of pre-2022 whole rocks and the majority of 2022 glasses (Fig. 7a). A subset of 2022 glasses clusters at lower SiO_2 concentrations, whereas pre-2022 glasses are slightly shifted toward higher SiO_2 concentrations, lying between the two experimental trends observed at high and low thermal conditions (Fig. 7a). The formation of more differentiated andesitic melts is consistent with the pre-2022 small-scale Surtseyan eruptions at Hunga volcano, which were fed by a shallower and more degassed magmatic reservoir compared to the climactic January 2022 eruption (Le Mevèl et al., 2023). The progressive decrease in CaO and MgO contents observed for natural products aligns with the experimental trend (Fig. 7b), supporting a genetic relationship between the pre-2022 and 2022 erupted magmas. This relationship appears to be primarily governed by the cotectic crystallization of clinopyroxene and plagioclase at low pressure. Our interpretation is supported by the broader findings of Adam et al. (2016), who integrated published experimental data for *liquidus* equilibria with representative arc magma compositions. On the $CaAl_2O_4$-silica-forsterite projection, whole rock compositions from volcanic islands in the northern Tonga arc (i.e., Tofua, Late, and Fonualei), show magma evolution along the 1 atm, low alkali cotectic involving clinopyroxene, plagioclase, and orthopyroxene. By extending this phase equilibrium framework to arc volcanoes worldwide, Adam et al. (2016) further observed that most silicic arc magmas differentiated at shallow depths (P = 100–300 MPa), regardless of total crustal thickness. This challenges the applicability of models that invoke repeated underplating and partial melting at the base of the arc crust as the primary mechanism for silicic magma generation, where a density barrier near the crust-mantle interface may facilitate the stalling of ascending basaltic magmas (cf. Annen et al., 2006).

Magnetite appears as the *liquidus* phase in our experiments, and its stability field significantly expands with decreasing temperature (Table 1 and Fig. 2). The incipient crystallization of magnetite lowers the FeO_{tot} content of experimental melts from ~7–8 wt% ($T > 1000$ °C) to ~6–4 wt% ($T = 1000$ °C). This depletion accounts for the discrepancy between experimental data and the typical higher total iron contents observed in most pre-2022 whole rocks (~9–11 wt% FeO_{tot}), as well as in matrix glasses from both pre-2022 (~10–12 wt% FeO_{tot}) and 2022 (~9–11 wt% FeO_{tot}) eruptions (Supplementary Material 1). As a result, most natural compositions show a clear tholeiitic affinity (Fig. 7c), whereas the experimental trend obtained at $T > 1000$ °C aligns along the boundary between the calc-alkaline and tholeiitic domains, reflecting a continuum differentiation between these two magmatic lineages. At T = 1000 °C, the evolutionary trend defined by the experimental glasses shifts distinctly toward a calc-alkaline character (Fig. 7c). Additionally, magnetite saturation increases the activity of silica in the melt (Toplis and Carroll, 1995), causing the initial SiO_2 content of the staring basaltic composition to rise from ~55 to ~57 wt% at the onset of crystallization (Fig. 7a). At $T = 1000$ °C, extensive magnetite crystallization produces silica-rich dacitic melts (~66–69 wt% SiO_2), which are not observed in either pre-2022 or 2022 eruptions at Hunga volcano (Fig. 7a). However, for the sake of completeness, we emphasize that low-temperature, magnetite-bearing phenocryst assemblages from dacitic eruptions on several Tongan islands (e.g., Fonualei, Late, and Metis Shoal) are thought to have originated from basaltic andesitic magmas by crystal-liquid fractionation processes (Ewart et al., 1973).

As modeled by Bohrson et al. (2014), the melt density is typically comparable to the bulk crystal density in magmatic systems, implying that volume fractions closely approximate mass fractions. Based on this relationship, mass balance calculations indicate that a substantial increase of magnetite content from 1 to 6 vol% in the experimental charges (Table 1) can enrich the SiO_2 content of the residual melt by ~3.5 wt%. Such enrichment accounts for the compositions of silica-rich dacitic melts obtained at $T = 1000$ °C and $H_2O^{melt} < 4$ wt% (Fig. 7a), when the crystallinity increases to 46 vol% (Table 1 and Fig. 2). Pyroclastic deposits from large-magnitude eruptions at Hunga volcano exhibit basaltic andesitic to weakly differentiated andesitic glass compositions (Le Mevèl et al., 2023). Their crystal contents never exceed 15 vol%, consistent with magma storage conditions characterized by temperatures of 1075–1130 °C and melt-water contents of 1–3 wt% (Table 1 and Fig. 2). In contrast, andesitic lava flows reach maximum SiO_2 contents of ~64 wt% and are dominated by plagioclase and clinopyroxene phenocrysts, with modal abundance up to 40 vol% (Brenna et al., 2022). To sustain such high crystal content at the low temperature of 1000 °C, our experiments indicate that the melt must dissolve more than 5 wt% water to sufficiently depress the *liquidus* and suppress further crystallization (Table 1 and Fig. 2). Nonetheless, most melt inclusion data report H_2O^{melt} contents between 0.5 and 3 wt% (Wu et al., 2025), thereby

constraining the formation of andesitic magmas to higher temperatures, typically ranging from 1025 to 1050 °C, as illustrated in Fig. 7a.

Magnetite is rare in volcanic products from the Hunga eruptions, occurring mainly in close textural association with clinopyroxene and plagioclase, either as glomerocrysts or as inclusions within silicate minerals, and only sporadically in the matrix glass of natural samples (Brenna et al., 2022). The compositions of natural grains (~80–88 wt% FeO^{mt}, ~8–16 $Mg\#^{mt}$, and ~0.1–0.7 $Cr\#^{mt}$) are generally comparable to those of experimental crystals. Their tendency to cluster at low FeO^{mt} and $Mg\#^{mt}$ indicates crystallization from the magma at $T \leq 1050$ °C, where natural magnetite compositions are more accurately reproduced in the present experiments. More broadly, phenocrysts of magnetite are documented exclusively in silica-rich andesitic and dacitic lava flows from Tongan islands. Least squares fractionation modeling of Ewart et al. (1973) suggests that magnetite segregation from primitive basaltic andesitic magmas plays a key role in controlling the systematic decrease in vanadium concentration observed in the more differentiated products.

The factors inhibiting magnetite stability in magmas erupted at Hunga volcano are not immediately apparent from our experimental results and the restricted range of data published on the natural products. Looking at phase equilibrium data from the literature, Nielsen et al. (1994) report phase equilibrium experiments conducted using as starting melt compositions a variety of natural basaltic lavas from different tectonic setting, including island arcs, mid-ocean ridges, and ocean islands, as well as basaltic andesitic and andesitic lava flows. Magnetite is present on the *liquidus* of all these melt compositions at P of 1 atm, T ranging from 1080 to 1129 °C, and fO_2 near the NNO buffer. Magnetite ceases to crystallize from ferrobasaltic to dacitic magmas only under more reduced conditions, ranging from ΔNNO-0.6 to ΔNNO-2.7 (Shepherd et al., 2022). The appearance temperature of magnetite is ~1100 °C at ΔNNO+0.7 in ferrobasaltic melts and its *liquidus* rises by ~30 °C per logfO_2 unit (Toplis and Carroll, 1995), consistent with magnetite crystallization observed at 1130 °C for our phase relations. Variations in melt composition may also strongly influence the crystallization of magnetite. In their experimental studies, Botcharnikov et al. (2005) and Berndt et al. (2005) investigated one ferrobasalt and two mid-ocean ridge basalts, respectively, differing primarily by up to ~4 wt % FeO_{tot}. Under equivalent P-T-fO_2-H_2O^{melt} conditions and using the same experimental apparatus, the ferrobasalt crystallizes magnetite on the *liquidus*, as documented here, and its stability is almost independent of the value of fO_2 and the activity of H_2O^{melt} (Botcharnikov et al., 2005). In contrast, magnetite does not appear as the *liquidus* phase of the two mid-ocean ridge basalts and only saturates the melt under highly oxidizing conditions (Berndt et al., 2005).

We also emphasize that in classical equilibrium crystallization experiments, crystals remain in contact with the residual melt and the value of fO_2 is buffered by the melt composition, including the dissolved water and the redox state imposed by experimental apparatus. Therefore, significant changes in fO_2 are not expected in the melt, as equilibrium crystallization occurs in a system closed to mass and volatile exchange with its surroundings. Conversely, magmas residing in dynamic subvolcanic environments undergo variable redox states driven by multiphase fractional crystallization, mixing, and loss of volatiles prior to or during eruption (Kelly and Cottrell, 2012). These processes lead to structural-chemical reactions that modify the ferric-ferrous ratio of the melt and the stability of magnetite throughout the entire fractional crystallization path (Christie et al., 1986). To elucidate how melt composition evolves by fractional crystallization across a range of redox conditions, from reducing to oxidizing, we performed nine sets of thermodynamic simulations using the rhyolite-MELTS code (v.1.2.0; Gualda et al., 2012). This version represents an updated and improved implementation of the original MELTS model (Ghiorso and Sack, 1995), incorporating corrections to phase saturation detection, the thermodynamic properties of the fluid phase, and energy convergence based on Gibbs free energy minimization. The starting melt composition was the same primitive basaltic andesite used in the experiments. Thermodynamic runs began at $T_{superliquidus}$ of 1250 °C and proceeded along a fractional crystallization path down to 900 °C, with the temperature decreased by 10 °C at each step. The fractional crystallization process was simulated at a constant P of 200 MPa, $H_2O^{melt}_{initial}$ of 1, 2, and 3 wt%, and fO_2 of ΔNNO-1.5, ΔNNO, and ΔNNO+1.5. Results from these calculations are provided in Supplementary Material 3. The mineral phases predicted by thermodynamic simulations are consistent with those observed in our experiments across the range of melt redox states and water contents. However, at $H_2O^{melt}_{initial}$ of 1 wt%, orthopyroxene is stable only under an oxygen fugacity of ΔNNO+1.5, whereas plagioclase oversteps the crystallization of clinopyroxene by 30 °C. When $H_2O^{melt}_{initial}$ rises to 3 wt%, this thermal offset decreases to 10 °C. Notably, an increase of $H_2O^{melt}_{initial}$ from 1 to 3 wt% lowers the saturation temperature of silicate minerals by ~60–80 °C, whereas the stability field of magnetite is only modestly reduced by ~20 °C. Conversely, an increase in fO_2 by three log units results in a dramatic increase in the saturation temperature of magnetite by ~110 °C, with negligible influence on the stability of silicate minerals. The amount of water dissolved in the melt increases gradually with the fractional crystallization of nominally anhydrous minerals, as observed by Ewart et al. (1998) during the geochemical evolution of magmas at the Tonga arc. For example, silica-rich andesitic melts (~64 wt% SiO_2) contain water contents varying from ~2 to ~6 wt %, as $H_2O^{melt}_{initial}$ increases from 1 to 3 wt%. The modeled fractional crystallization trends broadly reproduce the compositional variability of natural products from Hunga volcano, particularly in terms of $Na_2O + K_2O$ vs. SiO_2 and MgO vs. CaO. These diagrams, along with the FeO_{tot}/MgO vs. SiO_2 classification diagram of Miyashiro (1974), are presented in Supplementary Material 3. To illustrate the transition from tholeiitic to calk-alkaline affinity as a function of melt redox state and magnetite stability, selected key fractional crystallization trends are displayed in Fig. 7c. Under the more reducing condition of ΔNNO-1.5 and $H_2O^{melt}_{initial}$ between 1 and 2 wt%, the melt composition shifts from calc-alkaline to tholeiitic at ~57 wt% SiO_2. This transition is favored by delayed magnetite crystallization at temperatures ≤980 °C (Supplementary Material 3), leading to a gradual increase in both SiO_2 and FeO_{tot}/MgO ratio along two steep fractional crystallization trends (Fig. 7c). In contrast, under more oxidizing conditions, magnetite begins to crystallize earlier, at temperatures varying from 1010 to 1090 °C as the value of fO_2 increases from ΔNNO to ΔNNO+1.5 (Supplementary Material 3). Consequently, the modeled fractional crystallization trends exhibit a pronounced convex curvature toward silica enrichments in the melts at ~58 and ~60 wt% SiO_2 for $H_2O^{melt}_{initial}$ of 1 and 2 wt%, respectively (Fig. 7c). These deviations may lead the fractional crystallization trends to eventually cross the tholeiitic-calc-alkaline boundary in the diagram of Miyashiro (1974), depending on the degree of magnetite fractionation. Notably, at a given FeO_{tot}/MgO ratio, the silica enrichment observed in some 2022 glasses at Hunga volcano ($SiO_2 > 60$ wt%; Fig. 7c) requires fractional crystallization of magnetite under relatively oxidizing conditions. This finding is also in agreement with least squares fractionation modeling by Ewart et al. (1973), which attributes the formation of silica-rich andesites and dacites at the Tongan islands to magnetite segregation.

Zoning patterns in clinopyroxene and plagioclase phenocrysts at Hunga volcano testify to convective mixing regimes associated with the upward migration of recharge magmas across different crustal levels (Brenna et al., 2022). Under such dynamic conditions, magnetite saturation on the *liquidus* may be inhibited by fluctuations in fO_2 caused by the mixing of magmas with differing redox states and/or compositions. Rooted in early studies of natural volcanic systems (Anderson and Wright, 1972; Kress, 1997), this interpretation is also corroborated by experimental data on basaltic magmas (Berndt et al., 2005; Botcharnikov et al., 2005). Fractional crystallization, coupled with episodic recharge events of mafic magmas from depth, may reduce the stability

field of magnetite at shallow crustal levels, prompting clinopyroxene saturation on the *liquidus* and extensive plagioclase crystallization at low temperatures (Lange and Carmichael, 1996). The presence of matrix glasses in the 2022 eruptive products, characterized by variable proportions of vesicles, microlites, and water contents, further supports the mingling/mixing of magmas with distinct storage and degassing histories (Wu et al., 2025). Sulfur concentration in melt inclusions from 2022 eruptions also decreases with increasing melt differentiation, suggesting that sulfur degassing began during the early stages of magma crystallization (Wu et al., 2025). Importantly, Kelly and Cottrell (2012) integrated major-trace element concentrations and dissolved volatile contents in olivine-hosted melt inclusions with XANES spectroscopy measurements at the iron K-edge. For basaltic arc magmas, the authors found that multiphase fractional crystallization involving olivine ± clinopyroxene ± plagioclase does not necessarily result in increased melt $Fe^{3+}/\sum Fe$ ratios with decreasing MgO, as would be expected under more oxidizing magmatic conditions. Rather, the observed decrease in melt $Fe^{3+}/\sum Fe$ ratios correlates with declining sulfur concentrations, driven by electronic exchanges associated with conversion of dissolved S^{2-} to SO_2 gas. The eight-electron disparity between reduced sulfide (S^{2-}) and oxidized sulfate (S^{6+}) species facilitates electron transfer processes that shift iron in the melt toward its more reduced valence state during magmatic differentiation and degassing (Kelly and Cottrell, 2012; Sun and Yao, 2024). Consistently, $Fe^{3+}/\sum Fe$ ratios measured in melt inclusions and matrix glasses from tephra erupted at Kīlauea volcano (Hawai'i) show that melt inclusions entrapped at depth are more oxidized than the matrix glasses (Moussallam et al., 2016). Modeling data based on gas-melt equilibration for these basaltic magmas indicate that ~0.1 wt% sulfur degassing at pressures below 100 MPa can cause a reduction of iron in the melt, corresponding to a decrease in fO_2 of ~1 log unit (Moussallam et al., 2016). Gas chemistry measurements at the Kīlauea summit lava lake further support the interpretation of an integrated signal resulting from the mixing of oxidized gases exsolved from magmas stored at depth and reduced gases exsolved from magmas at the near surface (Roeder et al., 2004).

In the scenario described above, magma mixing, fractional crystallization, and volatile degassing/outgassing at Hunga volcano may collectively inhibit the formation of magnetite by controlling the bulk compositions and redox state of magmas across the plumbing system. Looking ahead, we recommend that future analytical efforts prioritize the quantification of $Fe^{3+}/\sum Fe$ ratios from XANES spectra of melt inclusions and matrix glasses from eruptions at Tongan islands. In the absence of high-resolution data on iron speciation within the erupted products, reconciling our experimental results with natural observations remains speculative. We tentatively propose that our findings reflect the redox conditions of relatively oxidized magmas stored at depth, prior to sulfur degassing at very shallow levels, an event that likely delays or even inhibits magnetite crystallization through the reduction of Fe in the melt. This interpretation is supported by the occurrence in the 2022 eruptions of large glomerocrysts (up to ~600 μm) of magnetite, clinopyroxene, and plagioclase phenocrysts in mutual textural relationship, suggesting crystallization within the deeper segments of the plumbing system. Furthermore, our interpretation aligns with volatile solubility modeling, which places the base of the main Hunga magma reservoir at ~150 MPa (~6 km depth) and its uppermost level at ~50 MPa (~2 km depth), as inferred from water contents in plagioclase-hosted melt inclusions and matrix glasses, respectively (Wu et al., 2025).

5. Conclusions

This study provides new experimental and thermodynamic constraints on the pre-eruptive magmatic conditions at Hunga volcano, defining how pressure (*P*), temperature (*T*), melt-water content (H_2O^{melt}), and oxygen fugacity (fO_2) mutually govern mineral phase stability, crystal-melt equilibria, and melt differentiation. The integrated analysis of experimental results with thermodynamic modeling, orthopyroxene-clinopyroxene thermometry, and plagioclase-based hygrometry reveals that Hunga magmas differentiated under polybaric-polythermal conditions within a vertically structured plumbing system extending from mid to shallow crustal levels. Cotectic crystallization of clinopyroxene and plagioclase plays a major role in magmatic differentiation, particularly by controlling the CaO and MgO contents of the residual melts, while the incipient crystallization of magnetite under oxidizing conditions lowers the FeO_{tot}/MgO ratio and increases the SiO_2 content.

Beyond the case of Hunga volcano, our results have broader implications for understanding magma differentiation and redox evolution at intra-oceanic arc volcanoes. The experimental dataset highlights that the interplay between *T* and H_2O^{melt} exerts first-order control on the cotectic crystallization of plagioclase and clinopyroxene, as well as the onset of orthopyroxene saturation. In contrast, fO_2 primarily governs the stability of magnetite and drives the transition from tholeiitic to calc-alkaline affinity of magmas. Collectively, these findings establish a quantitative framework to interpret mineral assemblages and melt compositions in other subduction-related volcanoes, linking mineral phase relations and compositions to melt differentiation. Additionally, our dataset provides a benchmark reference for thermodynamic modeling in arc settings. By constraining mineral-melt equilibria under experimentally calibrated P-T-fO_2-H_2O^{melt} conditions, this approach contributes to improving existing thermodynamic formulations and offers a solid foundation for testing and refining equilibrium crystallization models applicable across a wide range of magmatic systems and tectonic environments.

CRediT authorship contribution statement

Enrico Califano: Writing – review & editing, Writing – original draft, Investigation, Formal analysis, Data curation, Conceptualization. **Silvio Mollo:** Writing – review & editing, Writing – original draft, Supervision, Investigation, Funding acquisition, Data curation, Conceptualization. **Marco Brenna:** Writing – review & editing, Writing – original draft, Supervision, Investigation, Funding acquisition, Data curation, Conceptualization. **Alessio Pontesilli:** Writing – review & editing, Writing – original draft, Supervision, Data curation, Conceptualization. **Jie Wu:** Writing – review & editing, Writing – original draft, Data curation, Conceptualization. **Patricia Marks:** Writing – review & editing, Writing – original draft, Methodology. **Dennis Eul:** Writing – review & editing, Writing – original draft, Methodology. **Marcus Nowak:** Writing – review & editing, Writing – original draft, Methodology. **Shane J. Cronin:** Writing – original draft, Writing – review & editing. **Fabrizio Di Fiore:** Writing – review & editing, Writing – original draft, Methodology, Formal analysis. **Alessandro Vona:** Writing – review & editing, Writing – original draft, Formal analysis. **Sumith Abeykoon:** Writing – review & editing, Writing – original draft, Methodology, Formal analysis. **Danilo Di Genova:** Writing – review & editing, Writing – original draft, Methodology, Formal analysis. **Claudia Romano:** Writing – review & editing, Writing – original draft. **Piergiorgio Scarlato:** Writing – review & editing, Writing – original draft.

Declaration of competing interest

The authors declare that they have no known competing financial interests or personal relationships that could have appeared to influence the work reported in this paper.

Acknowledgements

M.B. and S.J.C. acknowledge funding from the Marsden Grant and the support of the NZ Ministry for Business, Innovation and Enterprise (MBIE) Endeavour Research Programme MFP-UOO2218 and MFP-UOA24103. D.D.G. acknowledges funding from the European Research Council (ERC) under the Horizon Europe 2020 research and innovation

programme (NANOVOLC, ERC Consolidator Grant #101044772). D.D. G. and S.A. acknowledge funding from the MUR-PRIN Project (CRYSTALlKIN, 2022L2APNR). A.V. acknowledges funding from the MUR-PRIN Project (#P20222BP7J). This paper benefited from thoughtful and constructive reviews by Rebecca deGraffenried and two anonymous reviewers. Marco Fiorentini is also acknowledged for his editorial guidance, which was very greatly appreciated.

Appendix A. Supplementary data

Supplementary data to this article can be found online at https://doi.org/10.1016/j.chemgeo.2026.123328.

Data availability

All data are included into the supplementary materials.

References

Adam, J., Turner, M., Hauri, E.H., Turner, S., 2016. Crystal/melt partitioning of water and other volatiles during the near-solidus melting of mantle peridotite: comparisons with non-volatile incompatible elements and implications for the generation of intraplate magmatism. Am. Mineral. 101, 876–888.

Aigner-Torres, M., Blundy, J., Ulmer, P., Pettke, T., 2007. Laser Ablation ICPMS study of trace element partitioning between plagioclase and basaltic melts: an experimental approach. Contrib. Mineral. Petrol. 153, 647–667.

Anderson, A.T., Wright, T.L., 1972. Phenocrysts and glass inclusions and their bearing on oxidation and mixing of basaltic magmas, Kilauea Volcano, Hawaii. Am. Mineral. 57, 188–216.

Annen, C., Blundy, J.D., Sparks, R.S.J., 2006. The genesis of intermediate and silicic magmas in deep crustal hot zones. J. Petrol. 47 (3), 505–539.

Astafyeva, E., Maletckii, B., Mikesell, T.D., Munaibari, E., Ravanelli, M., Coisson, P., Manta, F., Rolland, L., 2022. The 15 January 2022 Hunga Tonga eruption history as inferred from ionospheric observations. Geophys. Res. Lett. 49, e2022GL098827.

Barr, J.A., Grove, T.L., 2010. AuPdFe ternary solution model and applications to understanding the fO_2 of hydrous, high-pressure experiments. Contrib. Mineral. Petrol. 160, 631–643.

Berndt, J., Liebske, C., Holtz, F., Freise, M., Nowak, M., Ziegenbein, D., Hurkuck, W., Koepke, J., 2002. A combined rapid-quench and H2-membrane setup for internally heated pressure vessels: description and application for water solubility in basaltic melts. Am. Mineral. 87, 1717–1726.

Berndt, J., Koepke, J., Holtz, F., 2005. An experimental investigation of the influence of water and oxygen fugacity on differentiation of MORB at 200MPa. J. Petrol. 46 (1), 135–167.

Blander, M., 1972. Thermodynamic properties of orthopyroxenes and clinopyroxenes based on the ideal two-site model. Geochim. Cosmochim. Acta 36 (7), 787–799.

Blatter, D.L., Sisson, T.W., Hankins, W.B., 2013. Crystallization of oxidized, moderately hydrous arc basalt at midto lower-crustal pressures: implications for andesite genesis. Contrib. Mineral. Petrol. 166, 861–886.

Blundy, J.D., Falloon, T.J., Wood, B.J., Dalton, J.A., 1995. Sodium partitioning between clinopyroxene and silicate melts. J. Geophys. Res. 100 (B8), 15501–15515.

Bohrson, W., Spera, F.J., Ghiorso, M., Brown, G., Creamer, J.B., Mayfield, A., 2014. Thermodynamic model for energy-constrained open-system evolution of crustal magma bodies undergoing simultaneous recharge, assimilation and crystallization: the magma chamber simulator. J. Petrol. 55 (9), 1685–1717.

Bonechi, B., Perinelli, C., Gaeta, M., Fabbrizio, A., Petrelli, M., Strnad, L., 2021. High pressure trace element partitioning between clinopyroxene and alkali basaltic melts. Geochim. Cosmochim. Acta 305, 282–305.

Botcharnikov, R.E., Koepke, J., Holtz, F., Mccammon, C., Wilke, M., 2005. The effect of water activity on the oxidation and structural state of Fe in a ferro-basaltic melt. Geochim. Cosmochim. Acta 69 (21), 5071–5085.

Botcharnikov, R.E., Almeev, R.R., Koepke, J., Holtz, F., 2008. Phase relations and liquid lines of descent in hydrous ferrobasalt - implications for the Skaergaard intrusion and Columbia River flood basalts. J. Petrol. 49 (9), 1687–1727.

Brenna, M., Cronin, S.J., Smith, I.E.M., Pontesilli, A., Tost, M., Barker, S., Tonga'onevai, S., Kula, T., Vaiomounga, R., 2022. Post-caldera volcanism reveals shallow priming of an intra-oceanic arc andesitic caldera: Hunga volcano, Tonga, SW Pacific. Lithos 412–413, 106614.

Bryan, W.B., Stice, G.D., Ewart, A., 1972. Geology, petrography, and geochemistry of the volcanic islands of Tonga. J. Geophys. Res. 77, 8.

Burnham, C.W., 1979. The importance of volatile constituents. In: Yoder, H.S. (Ed.), The Evolution of the Igneous Rocks. Princeton University Press, Princeton, NJ, pp. 1077–1084.

Canil, D., O'Neill, H.S.C., 1996. Distribution of ferric iron in some Upper-Mantle Assemblages. J. Petrol. 37 (3), 609–635.

Christie, D.M., Carmichael, I.S.E., Langmuir, C.H., 1986. Oxidation states of mid-ocean ridge basalt glasses. Earth Planet. Sci. Lett. 19, 397–411.

Contreras-Reyes, E., Grevemeyer, I., Watts, A.B., Flueh, E.R., Peirce, C., Moeller, S., Papenberg, C., 2011. Deep seismic structure of the Tonga subduction zone: implications for mantle hydration, tectonic erosion, and arc magmatism. J. Geophys. Res. 116, B10103. https://doi.org/10.1029/2011JB008434.

Cooper, L., Plank, T., Arculus, R., Hauri, E., Kelley, K.A., 2022. Arc-backarc exchange along the Tonga–Lau system: constraints from volatile elements. J. Petrol. 63, 1–25.

Crawford, W.C., Hildebrand, J.A., Dorman, L.M., Webb, S.C., Wiens, D.A., 2003. Tonga Ridge and Lau Basin crustal structure from seismic refraction data. J. Geophys. Res. 108 (B4), 2195. https://doi.org/10.1029/2001JB001435.

Cronin, S.J., Brenna, M., Smith, I.E.M., Barker, S.J., Tost, M., Ford, M., Tonga'onevai, S., Kula, T., Vaiomounga, R., 2017. New volcanic island unveils explosive past. Eos 98.

Davidson, P.M., Lindsley, D.H., 1989. Thermodynamic analysis of pyroxene-olivine-quartz equilibria in the system CaO-MgO-FeO-SiO_2. Am. Mineral. 74 (1–2), 18–30.

De Grave, E., Eeckhout, S.G., 2003. 57Fe Mössbauer-effect studies of Ca-rich, Fe-bearing clinopyroxenes: part III. diopside. Am. Mineral. 88, 1145–1152.

Del Bello, E., Mollo, S., Scarlato, P., von Quadt, A., Forni, F., Bachmann, O., 2014. New petrological constraints on the last eruptive phase of the Sabatini Volcanic District (central Italy): clues from mineralogy, geochemistry, and Sr–Nd isotopes. Lithos 205, 28–38.

Devine, J.D., Gardner, J.E., Brack, H.P., Layne, G.D., Rutherford, M.J., 1995. Comparison of microanalytical methods for estimating H_2O contents of silicic volcanic glasses. Am. Mineral. 80, 319–328.

Di Fiore, F., Mollo, S., Vona, A., MacDonaldd, A., Ubide, T., Nazzari, M., Romano, C., Scarlato, P., 2021. Kinetic partitioning of major and trace cations between clinopyroxene and phonotephritic melt under convective stirring conditions: new insights into clinopyroxene sector zoning and concentric zoning. Chem. Geol. 584, 120531.

Di Genova, D., Sicola, S., Romano, C., Vona, A., Fanara, S., Spina, L., 2017. Effect of iron and nanolites on Raman spectra of volcanic glasses: a reassessment of existing strategies to estimate the water content. Chem. Geol. 475, 76–86.

Dickenson, M.P., Hess, P.C., 1986. The structural role and homogeneous redox equilibria of iron in peraluminous, metaluminous and peralkaline silicate melts. Contrib. Mineral. Petrol. 92, 207–217.

Dolfi, D., Trigila, R., 1983. Clinopyroxene solid solutions and water in magmas: results in the system phonolitic tephrite-H20. Mineral. Mag. 47, 347–351.

Droop, G.T.R., 1987. A general equation for estimating Fe 3+ concentrations in ferromagnesian silicates and oxides from microprobe analyses, using stoichiometric criteria. Mineral. Mag. 51, 431–435.

Duan, X., 2014. A general model for predicting the solubility behavior of H2O–CO2 fluids in silicate melts over a wide range of pressure, temperature and compositions. Geochim. Cosmochim. Acta 125, 582–609.

Ewart, A., Bryan, W.B., Gill, J.B., 1973. Mineralogy and geochemistry of the younger volcanic islands of Tonga, S.W. Pacific. J. Petrol. 14, 429–465.

Ewart, A., Collerson, K.D., Regelous, M., Wendt, J.I., Niu, Y., 1998. Geochemical evolution within the Tonga–Kermadec–Lau Arc–back-arc systems: the role of varying mantle wedge composition in space and time. J. Petrol. 39, 331–368.

Fabbrizio, A., Schmidt, M.W., Petrelli, M., 2021. Effect of fO_2 on Eu partitioning between clinopyroxene, orthopyroxene and basaltic melt: development of a Eu^{3+}/Eu^{2+} oxybarometer. Chem. Geol. 559, 119967.

Flowers, G.C., 1979. Correction of Holloway's (1977) Adaptation of the modified Redlich-Kwong equation of state for calculation of the fugacities of molecular species in supercritical fluids of geologic interest. Contrib. Mineral. Petrol. 69, 315–318.

Ganguly, J., 1982. Mg-Fe order-disorder in ferromagnesian silicates II. Thermodynamics, kinetics, and geological applications. In: Saxena, S.K. (Ed.), Advances in Physical Geochemistry, Vol vol. 2. Springer, Berlin Heidelberg New York, pp. 58–59.

Ganguly, J., Saxena, S.K., 1987. Mixtures and Mineral Reactions. Springer-Verlag, Berlin-Heidelberg-New York.

Gatliff, R.W., Helu, S., Singh, R., 1991. Annual report of the world volcanic eruptions in 1988. Bull. Volcanol. 53, 1–108.

Ghiorso, M.S., Sack, R.O., 1995. Chemical mass transfer in magmatic processes IV. A revised and internally consistent thermodynamic model for the interpolation and extrapolation of liquid-solid equilibria in magmatic systems at elevated temperatures and pressures. Contrib. Mineral. Petrol. 119, 197–212.

Glazner, A.F., 1984. Activities of olivine and plagioclase components in silicate melts and their application to geothermometry. Contrib. Mineral. Petrol. 88, 260–268.

Grove, T.L., Baker, M.B., 1984. Phase equilibrium controls on the tholeiitic versus calc-alkaline differentiation trends. J. Geophys. Res. 89B, 3253–3274.

Gualda, G.A.R., Ghiorso, M.S., Lemons, R.V., Carley, T.L., 2012. Rhyolite-MELTS: a modified calibration of MELTS optimized for silica-rich, fluid-bearing magmatic systems. J. Petrol. 53 (5), 875–890.

Helgeson, H.C., Delany, J.M., Nesbitt, H.W., Bird, D.K., 1978. Summary and critique of thermodynamic properties of rock-forming minerals. Am. J. Sci. 278A, 1–229.

Holland, T.J.B., 1983. The experimental determination of activities in disordered and short-range ordered jadeitic pyroxenes. Contrib. Mineral. Petrol. 82, 214–220.

Holloway, J.R., 1977. Fugacity and activity of molecular species in supercritical fluids. Thermodyn. Geol. 161–181.

Holloway, J.R., Blank, J.G., 1994. Application of experimental results to C-O-H species in natural melts. Rev. Mineral. Geochem. 30 (1), 187–230.

Huebner, J.S., Sato, M., 1970. The oxygen fugacity-temperature relationships of manganese oxide and nickel oxide buffers. Am. Mineral. 55, 934–952.

Humphreys, M.C.S., Edmonds, M., Klöcking, M.S., 2016. The validity of plagioclase-melt geothermometry for degassing-driven magma crystallization. Am. Mineral. 101, 769–779.

Iacovino, K., Moore, G., Roggensack, K., Oppenheimer, C., Kyle, P., 2013. H_2O–CO_2 solubility in mafic alkaline magma: applications to volatile sources and degassing behavior at Erebus volcano, Antarctica. Contrib. Mineral. Petrol. 166, 845–860.

Irvine, T.N., Baragar, W.R.A., 1971. A guide to the chemical classification of the common volcanic rocks. Can. J. Earth Sci. 8, 523.

Kelly, K.A., Cottrell, E., 2012. The influence of magmatic differentiation on the oxidation state of Fe in a basaltic arc magma. Earth Planet. Sci. Lett. 329-330, 109–121.
King, P.L., Hervig, R.L., Holloway, J.R., Delaney, J.S., Dyar, M.D., 2000. Partitioning of $Fe3^{+}/Fe^{total}$ between amphibole and basanitic melt as a function of oxygen fugacity. Earth Planet. Sci. Lett. 178, 97–112.
Kress, V., 1997. Magma mixing as a source for Pinatubo sulphur. Nature 389, 591–593.
Kretz, R., 1981. Site-occupancy interpretation between orthopyroxene of the distribution of Mg and Fe and clinopyroxene in metamorphic rocks. Can. Mineral. 19, 493–500.
Kubota, T., Saito, T., Nishida, K., 2022. Global fast-traveling tsunamis driven by atmospheric Lamb waves on the 2022 Tonga eruption. Science 377, 91–94.
Lange, R.A., Carmichael, I.S.A., 1996. The Aurora volcanic field, California-Nevada: oxygen fugacity constraints on the development of andesitic magma. Contrib. Mineral. Petrol. 125, 167–185.
Lange, R.A., Frey, H.M., Hector, J., 2009. A thermodynamic model for the plagioclase-liquid hygrometer/thermometer. Am. Mineral. 94, 494–506.
Le Bas, M.J., Le Maitre, R.W., Streckeisen, A., Zanettin, B., 1986. A chemical classification of volcanic rocks based on the total alkali-silica diagram. J. Petrol. 27 (3), 745–750.
Le Mevèl, H., Miller, C.A., Ribó, M., Cronin, S.J., Kula, T., 2023. The magmatic system under Hunga volcano before and after the 15 January 2022 eruption. Sci. Adv. 9, 3156.
Lindsley, D.H., Grover, J.E., Davidson, P.M., 1981. The thermodynamics of the $Mg_2Si_2O_6$-$CaMgSi_2O_6$ join: a review and an improved model. Adv. Phys. Geochem. 1, 149–175.
Long, D.A., 1977. Raman Spectroscopy. McGraw-Hill, New York, p. 276.
Magnien, V., Neuville, D.R., Cormier, L., Roux, J., Hazemann, J.-L., De Ligny, D., Pascarelli, S., Vickridge, I., Pinet, O., Richet, P., 2008. Kinetics and mechanisms of iron redox reactions in silicate melts: the effects of temperature and alkali cations. Geochim. Cosmochim. Acta 72, 2157–2168.
Marks, P.L., Nowak, M., 2025. Vesiculation dynamics - part 1: decompression-induced H_2O vesicle formation in the Lower Laacher See phonolitic melt. Eur. J. Mineral. 37, 385–412.
Marxer, F., Ulmer, P., Müntener, O., 2022. Polybaric fractional crystallisation of arc magmas: an experimental study simulating trans-crustal magmatic systems. Contrib. Mineral. Petrol. 177, 3.
Masotta, M., Freda, C., Paul, T.A., Moore, G.M., Gaeta, M., Scarlato, P., Troll, V.R., 2012. Low pressure experiments in piston cylinder apparatus: calibration of newly designed 25 mm furnace assemblies to P=150 MPa. Chem. Geol. 312–313, 74–79.
Masotta, M., Mollo, S., Freda, C., Gaeta, M., Moore, G., 2013. Clinopyroxene–liquid thermometers and barometers specific to alkaline differentiated magmas. Contrib. Mineral. Petrol. 166, 1545–1561.
McCanta, M.C., Dyar, M.D., Rutherford, M.J., Delaney, J.S., 2004. Iron partitioning between basaltic melts and clinopyroxene as a function of oxygen fugacity. Am. Mineral. 89, 1685–1693.
McGuire, A.V., Dyar, M.D., Ward, K.A., 1989. Neglected Fe^{3+}/Fe^{2+} ratios - a study of Fe^{3+} content of megacrysts from alkali basalts. Geology 17, 687–690.
Miyashiro, A., 1974. Volcanic rock series and tectonic setting. Annu. Rev. Earth Planet. Sci. 3, 251.
Mollo, S., Hammer, J.E., 2017. Dynamic crystallization in magmas. In: Heinrich, W., Abart, R. (Eds.), Mineral Reaction Kinetics: Microstructures, Textures, Chemical and Isotopic Signatures, EMU Notes in Mineralogy, vol. 16. The Geological Society / The Mineralogical Society, London, pp. 373–418.
Mollo, S., Putirka, K., Iezzi, G., Del Gaudio, P., Scarlato, P., 2011. Plagioclase–melt (dis) equilibrium due to cooling dynamics: implications for thermometry, barometry and hygrometry. Lithos 125, 221–235.
Mollo, S., Putirka, K., Iezzi, G., Scarlato, P., 2013a. The control of cooling rate on titanomagnetite composition: implications for a geospeedometry model applicable to alkaline rocks from Mt. Etna volcano. Contrib. Mineral. Petrol. 165, 457–475.
Mollo, S., Putirka, K., Misiti, V., Soligo, M., Scarlato, P., 2013b. A new test for equilibrium based on clinopyroxene-melt pairs: clues on the solidification temperatures of Etnean alkaline melts at post-eruptive conditions. Chem. Geol. 352, 92–100.
Mollo, S., Giacomoni, P.P., Andronico, D., Scarlato, P., 2015. Clinopyroxene and titanomagnetite cation redistributions at Mt. Etna volcano (Sicily, Italy): footprints of the final solidification history of lava fountains and lava flows. Chem. Geol. 406, 45–54.
Mollo, S., Blundy, J., Scarlato, P., De Cristofaro, S.P., Tecchiato, V., Di Stefano, F., Vetere, F., Holtz, F., Bachmann, O., 2018. An integrated P-T-H2O-lattice strain model to quantify the role of clinopyroxene fractionation on REE+Y and HFSE patterns of mafic alkaline magmas: application to eruptions at Mt. Etna. Earth-Sci. Rev. 185, 32–56.
Mollo, S., Di Fiore, F., MacDonald, A., Ubide, T., Pontesilli, A., Giuliani, G., Vona, A., Romano, C., Scarlato, P., 2024. Thermodynamics and kinetics of cation partitioning between plagioclase and trachybasaltic melt in static and dynamic systems: a reassessment of the lattice strain and electrostatic energies of substitution. Geochim. Cosmochim. Acta 384, 27–43.
Moore, G., Carmichael, I.S.E., 1998. The hydrous phase equilibria (to 3 kbar) of an andesite and basaltic andesite from western Mexico: constraints on water content and conditions of phenocryst growth. Contrib. Mineral. Petrol. 130, 304–319.
Morimoto, N., 1988. Nomenclature of pyroxene. Am. Mineral. 73, 1123–1133.
Moschini, P., Mollo, S., Gaeta, M., Fanara, S., Nazzari, M., Petrone, C.M., Scarlato, P., 2021. Parameterization of clinopyroxene growth kinetics via crystal size distribution (CSD) analysis: insights into the temporal scales of magma dynamics at Mt. Etna volcano. Lithos 396–397, 106225.
Moschini, P., Mollo, S., Pontesilli, A., Nazzari, M., Petrone, C.M., Fanara, S., Vona, A., Gaeta, M., Romano, C., Scarlato, P., 2023. A review of plagioclase growth rate and compositional evolution in mafic alkaline magmas: guidelines for thermometry, hygrometry, and timescales of magma dynamics at Stromboli and Mt. Etna. Earth-Sci. Rev. 240, 104399.
Moussallam, Y., Edmonds, M., Scaillet, B., Peters, N., Gennaro, E., Sides, I., Oppenheimer, C., 2016. The impact of degassing on the oxidation state of basaltic magmas: a case study of Kılauea volcano. Earth Planet. Sci. Lett. 450, 317–325.
Mungall, J.E., Dingwell, D.B., Chaussidon, M., 1999. Chemical diffusivities of 18 trace elements in granitoid melts. Geochim. Cosmochim. Acta 63 (17), 2599–2610.
Namur, O., Charlier, B., Toplis, M.J., Auwera, J.V., 2012. Prediction of plagioclase-melt equilibria in anhydrous silicate melts at 1-atm. Contrib. Mineral. Petrol. 163, 133–150.
Neave, D.A., Stewart, A.G., Hartley, M.E., McCammon, C., 2024. Re-evaluating stoichiometric estimates of iron valence in magmatic clinopyroxene crystals. Contrib. Mineral. Petrol. 179, 5.
Newton, R.C., Haselton, H.T., 1981. Thermodynamics of the garnet—plagioclase—Al2SiO5—quartz geobarometer. Adv. Phys. Geochem. 1, 131–147.
Nielsen, R.L., Forsythe, L.M., Gallahan, W.E., Fisk, M.R., 1994. Major- and trace-element magnetite-melt equilibria. Chem. Geol. 117 (1–4), 167–191.
Perinelli, C., Mollo, S., Gaeta, M., De Cristofaro, S.P., Palladino, D.M., Armienti, P., Scarlato, P., Putirka, K.D., 2016. An improved clinopyroxene-based hygrometer for Etnean magmas and implications for eruption triggering mechanisms. Am. Mineral. 101, 2774–2777.
Perkins, D., Vielzeuf, D., 1992. Experimental investigation of Fe-Mg distribution between olivine and clinopyroxene: implications for mixing properties of Fe-Mg in clinopyroxene and garnet-clinopyroxene thermometry. Am. Mineral. 77, 774–783.
Pontesilli, A., Masotta, M., Nazzari, M., Mollo, S., Armienti, P., Scarlato, P., Brenna, M., 2019. Crystallization kinetics of clinopyroxene and titanomagnetite growing from a trachybasaltic melt: new insights from isothermal time-series experiments. Chem. Geol. 510, 113–129.
Powell, R., 1978. The thermodynamics of pyroxene geotherms. Phil. Trans. R. Soc. Lond. A 288, 457–469.
Powell, M., Powell, R., 1974. An olivine-clinopyroxene geothermometer. Contrib. Mineral. Petrol. 48, 249–263.
Proud, S.R., Prata, A.T., Schmauß, S., 2022. The January 2022 eruption of Hunga Tonga-Hunga Ha'apai volcano reached the mesosphere. Science 378, 554–557.
Putirka, K.D., 2005. Igneous thermometers and barometers based on plagioclase + liquid equilibria: tests of some existing models and new calibrations. Am. Mineral. 90, 336–346.
Putirka, K.D., 2008. Thermometers and Barometers for Volcanic Systems. Rev. Mineral. Geochem. 69, 61–120.
Putirka, K.D., 2016. Rates and styles of planetary cooling on Earth, Moon, Mars, and Vesta, using new models for oxygen fugacity, ferric-ferrous ratios, olivine-liquid Fe-Mg exchange, and mantle potential temperature. Am. Mineral. 101, 819–840.
Putirka, K.D., Mikaelian, H., Ryerson, F., Shaw, H., 2003. New clinopyroxene-liquid thermobarometers for mafic, evolved, and volatile-bearing lava compositions, with applications to lavas from Tibet and the Snake River Plain, Idaho. Am. Mineral. 88, 1542–1554.
Robie, R.A., Hemingway, B.S., Fisher, J.R., 1978. Thermodynamic properties of minerals and related substances at 298.15 K and 1 bar (10^5 pascals) pressure and at higher temperatures. US Geol. Surv. Bull. 1452, 456 p. (Reprinted in 1979).
Roeder, P.L., Thornber, C., Poustovetov, A., Grant, A., 2004. Reply to comment on paper: 'morphology and composition of spinel in Puu Oo lava (1996–1998), Kilauea volcano, Hawaii'-enigmatic discrepancies between lava and gas-based fO_2 determinations of Puu Oo lava. J. Volcanol. Geotherm. Res. 134, 245–248.
Rossman, G.R., 1980. Pyroxene spectroscopy. Rev. Mineral. Geochem. 7, 93–115.
Sack, R.O., 1980. Some Constraints on the Thermodynamic Mixing Properties of Fe-Mg Orthopyroxenes and Olivines. Contrib. Mineral. Petrol. 71, 257–269.
Sack, R.O., Carmichael, I.S.E., 1984. Fe^2-Mg^2 and $TiAl_2$-$MgSi_2$ exchange reactions between clinopyroxenes and silicate melts. Contrib. Mineral. Petrol. 85, 103–115.
Sack, R.O., Ghiorso, M.S., 1994. Thermodynamics of multicomponent pyroxenes: II. Phase relations in the quadrilateral. Contrib. Mineral. Petrol. 116, 287–300.
Saxena, S.K., Ghose, S., 1971. Mg^{2+}-Fe^{2+} order-disorder and the thermodynamics of the orthopyroxene crystalline solution. Am. Mineral. 56, 532–559.
Schellart, W.P., Lister, G.S., Toy, V.G., 2006. A late cretaceous and Cenozoic reconstruction of the Southwest Pacific region: tectonics controlled by subduction and slab rollback processes. Earth Sci. Rev. 76, 191–233.
Shepherd, K., Namur, O., Toplis, M.J., Devidal, J.-L., Charlier, B., 2022. Trace element partitioning between clinopyroxene, magnetite, ilmenite and ferrobasaltic to dacitic magmas: an experimental study on the role of oxygen fugacity and melt composition. Contrib. Mineral. Petrol. 177, 90.
Sisson, T.W., Grove, T.L., 1993. Experimental investigations of the role of H20 in calc-alkaline differentiation and subduction zone magmatism. Contrib. Mineral. Petrol. 113, 143–166.
Sun, C., Yao, L., 2024. Redox equilibria of iron in low- to high-silica melts: a simple model and its applications to C-H-O-S degassing. Earth Planet. Sci. Lett. 638, 118742.
Thompson Jr., J.B., 1969. Chemical reactions in crystals. Am. Mineral. 54, 341–375.
Tommasini, S., Bindi, L., Savia, L., Mangler, M.F., Orlando, A., Petrone, C.M., 2022. Critical assessment of pressure estimates in volcanic plumbing systems: the case study of Popocatepetl volcano, Mexico. Lithos 408-409, 106540.
Toplis, M.J., Carroll, M.R., 1995. An experimental study of the influence of oxygen fugacity on Fe-Ti oxide stability, phase relations, and mineral—melt equilibria in ferro-basaltic systems. J. Petrol. 36 (5), 1137–1170.
Vergoz, J., Hupe, P., Listowski, C., Le Pichon, A., Garcés, M.A., Marchetti, E., Labazuy, P., Ceranna, L., Pilger, C., Gaebler, P., Näsholm, S.P., Brissaud, Q., Poli, P., Shapiro, N.,

De Negri, R., Mialle, P., 2022. IMS observations of infrasound and acoustic-gravity waves produced by the January 2022 volcanic eruption of Hunga, Tonga: a global analysis. Earth Planet. Sci. Lett. 591, 117639.
Waters, L.A., Lange, R.A., 2015. An updated calibration of the plagioclase-liquid hygrometer-thermometer applicable to basalts through rhyolites. Am. Mineral. 100, 2172–2184.
Wilke, M., Behrens, H., 1999. The dependence of the partitioning of iron and europium between plagioclase and hydrous tonalitic melt on oxygen fugacity. Contrib. Mineral. Petrol. 137, 102–114.
Wood, B.J., Fraser, D.G., 1976. Elementary Thermodynamics for Geologists, 303. Oxford University Press, Oxford.
Wood, B.J., Holland, T.J.B., Newton, R.C., Kleppa, O.J., 1980. Thermochemistry of jadeite-diopside pyroxenes. Geochim. Cosmochim. Acta 44 (9), 1363–1371.
Wright, C.J., Hindley, N.P., Alexander, M.J., Barlow, M., Hoffmann, L., Mitchell, C.N., Prata, F., Bouillon, M., Carstens, J., Clerbaux, C., Osprey, S.M., Powell, N., Randall, C.E., Yue, J., 2022. Surface-to-space atmospheric waves from Hunga Tonga–Hunga Ha'apai eruption. Nature 609.
Wu, J., Cronin, S.J., Brenna, M., Park, S., Pontesilli, A., Ukstins, I.A., Adams, D., Paredes-Marino, J., Hamilton, K., Huebsch, M., Gonzalez-Garcia, D., Firth, C., White, J.D.L., Nichols, A.R.L., Plank, T., Vongsvivut, J., Klein, A., Ramos, F., Latu'ila, F., Kula, T., 2025. Low sulfur emissions from 2022 Hunga eruption due to seawater–magma interactions. Nat. Geosci. 18, 518–524.
Wu, J., Cronin, S.J., Brenna, M., Paredes-Mariño, J., Park, S.H., Huebsch, M., Pontesilli, A., Firth, C., Adams, D., Ubide, T., Hamilton, K., MacDonald, A., Califano, E., White, J.D.L., Plank, T., Ribó, M., Ukstins, I., Ramos, F., Mollo, S., Kim, J., Latu'ila, F., Kula, T., Vaiomounga, R., 2026. What triggered the catastrophic 15 January 2022 Hunga eruption? Earth Planet. Sci. Lett. (in review).
Yuen, D.A., Scruggs, M.A., Spera, F.J., Zheng, Y., Hu, H., McNutt, S.R., Thompson, G., Mandli, K., Keller, B.R., Wei, S.S., Peng, Z., Zhou, Z., Mulargia, F., Tanioka, Y., 2022. Under the surface: pressure-induced planetary-scale waves, volcanic lightning, and gaseous clouds caused by the submarine eruption of Hunga Tonga-Hunga Ha'apai volcano. Earthq. Res. Adv. 2, 100134.